Tectonophysics 880 (2024) 230337

Contents lists available at ScienceDirect

Tectonophysics

journal homepage: www.elsevier.com/locate/tecto

Fairweather transform boundary Oligocene to present orogenesis: Fairweather Range vertical extrusion and rotation of the Yakutat microplate at ca. 3 Ma

Jeff Apple Benowitz [a,*], Richard Lease [b], Peter J. Haeussler [b], Terry Pavlis [c], Michael Everett Mann [d]

[a] GeoSep Services, 1521 Pine Cone Road, Moscow, ID 83843, USA
[b] U.S. Geological Survey, Alaska Science Center, Anchorage, AK 99508, USA
[c] University of Texas, El Paso, TX 79968, USA
[d] Department of Earth, Environmental and Planetary Sciences, Brown University, Providence, RI, USA

ARTICLE INFO

Keywords:
Transform boundary tectonics
Microplate plate relative motion change
Vertical extrusion
Thermochronology
Double-indenter tectonics
Oblique-slip

ABSTRACT

Oblique-slip along transform fault boundaries is often partitioned between a strike-slip system and thrust faults that accommodate contraction. However, topography along the Yakutat-North American transform (Fairweather fault), is asymmetric with low-terrain above active thrusts on the western, Yakutat side of the transform and high topography on the continental side with peaks >4500 m (Mount Fairweather: 4671 m) to the west of the Border Ranges fault, limited recorded earthquakes >M4, and no apparent reverse faults to generate the highest terrain. In this study we compile, for the first time, published U-Pb zircon, ^{40}Ar/^{39}Ar and K-Ar (hornblende, muscovite, and biotite) and U-Th/He and fission-track (zircon and apatite) bedrock ages (109) from 75 samples to investigate the exhumation history of the Fairweather Range region, complemented by a published detrital sample (ZFT and AFT) and 13 new ^{40}Ar/^{39}Ar (hornblende, biotite, and K-feldspar) ages on 9 bedrock samples from both sides of the Fairweather fault. Additionally, we examined published seismicity and geodetic data of the Fairweather region and assessed if plate paleo-vectors correlate with the cooling history of the Fairweather Range. Cooling age, seismic, and block-motion patterns indicate the Fairweather Range has been vertically extruded between the Fairweather and the Border Ranges faults as a coherent block since ca. 25 Ma. The pre-6 Ma Pacific plate motion (N30°W) aligns with the N33°W strike of the Fairweather Fault whereas a hypothetical pre-6 Ma Yakutat microplate paleo-vector of (N39°W) does not: indicating a post-6 Ma timing for Yakutat microplate counter-clockwise rotation (9°). We infer that rotation and impingement of the Yakutat microplate along the Fairweather fault at ca. 3 Ma led to the development of the Fairweather restraining bend and increased cooling rates. The resultant thickened Fairweather welt and the ~30 km thick southeast end of the Yakutat microplate compounded double-indenter tectonics into Alaska's southeast convergent corner

1. Introduction

Strike-slip faults by definition are faults in which the majority of movement is parallel to the strike of the fault along an assumed near vertical fault plane (Crowell, 1974), yet across the globe many of the highest mountains and deepest exhumed rocks occur along these wrench structures (e.g. Karakorum Range; Valli et al., 2007; e.g. Alaska Range; Benowitz et al., 2019, 2022a). Vertical tectonics along strike-slip faults is often a result of oblique convergence and is commonly linked to mapped and inferred reverse splay fault systems, which are often described as flower (Harding, 1985) or palm tree structures (Sylvester, 1988). The San Andreas fault is a classic strike-slip fault, yet at least locally the fault plane is far from vertical (Fuis et al., 2012). Furthermore, oblique-slip on the master strand of the San Andreas fault is responsible for some of the most rapid exhumation rates along the entire fault system (Fattaruso et al., 2014) and associated large-scale block tilting (Dorsey and Langenheim, 2015).

Similarly, the Alpine fault of New Zealand is a comparable transpressional transform system but shows different structural patterns. The Alpine fault is decidedly "one-sided" with rapid exhumation and high

---

* Corresponding author.
E-mail address: jeffapplebenowitz@gmail.com (J.A. Benowitz).

https://doi.org/10.1016/j.tecto.2024.230337
Received 7 November 2023; Received in revised form 30 April 2024; Accepted 1 May 2024
Available online 6 May 2024

mountains east of the fault, low-terrain to the west, and a moderate fault dip towards the upthrown (eastern) side of the fault (Little et al., 2005; Herman et al., 2009; Norris and Toy, 2014). Paired faults along strike-slip faults can also promote vertical extrusion of coherent crustal blocks (Moser et al., 2017; Moulin and Cowgill, 2023; Roquer et al., 2023), but how this process operates and under what boundary conditions remains an open question. Thus, oblique-slip along the master strand of strike-slip faults during orogenesis deserves further consideration.

The Fairweather Range (Mount Fairweather; 4671 m) lays west of the Border Ranges fault, along the inboard, east side of the Fairweather transform boundary of southeastern Alaska, and in part on the convex side of a stable restraining bend (Lease et al., 2021) (Figs. 1–5). On the concave or west side of the Fairweather fault, the topography is generally at low elevations and rises towards the fault trace as well as northward, along strike. The ocean shoreline is around 10 km west of the fault and topography rises to around 1000 m about 2.5 km west of the fault, and only locally reaches heights of 1684 m (Mount Reaburn) (Figs. 3–5). The long-term horizontal slip rate of the Fairweather fault has been estimated through thermochronology to be 54 km/Myr, with short-term (< 1 Ma) exhumation rates as high as ~10 km/Myr where crustal material passes through the restraining bend (Lease et al., 2021). Quaternary exhumation rates on the convex side of the restraining bend, where topography is higher, are slower at ~2 km/Myr (McAleer et al., 2009; Lease et al., 2021). The overall history of vertical tectonics of the Fairweather Range, since the inception of the modern Fairweather fault inferred to be around 30 Ma (Plafker et al., 1994), has not previously been evaluated.

We applied ^{40}Ar/^{39}Ar thermochronology (hornblende, biotite, and K-feldspar; 13 ages total; Table S1A, B, C, D, E) on 9 rock samples from both sides of the Fairweather fault and compiled published U-Pb zircon, ^{40}Ar/^{39}Ar, and K-Ar (hornblende, muscovite, and biotite) and zircon fission-track and U-Th/He, apatite fission track, and apatite U-Th/He cooling ages (109 bedrock ages; 2 detrital fission track ages; 76 samples total; Table S1F and G). Additionally, we re-evaluated published geodetic (Elliott and Freymueller, 2020) and seismic data from the Fairweather fault corridor (Table S1H and I). We integrated these published and new data sets to investigate the effect of Pacific plate vector changes and potential Yakutat microplate rotation on Fairweather Range exhumation patterns, as well as the direct role of the Fairweather and the Border Ranges faults in the exhumation of the Fairweather Range.

2. Tectonic setting

2.1. Queen Charlotte-Fairweather transform boundary

The initiation age of the Queen Charlotte transform system is not well constrained, but was likely related to a Pacific plate vector (~20 to ~40° counter-clockwise) change at ca. 50 Ma (Rohr and Currie, 1997) constrained by comparing multiple hot-spot tracks (Torsvik et al., 2017; Finlayson et al., 2018; Gaastra et al., 2022) and plate circuit reconstructions (Doubrovine and Tarduno, 2008). The Queen Charlotte transform system is involved in the northward translation of the Yakutat

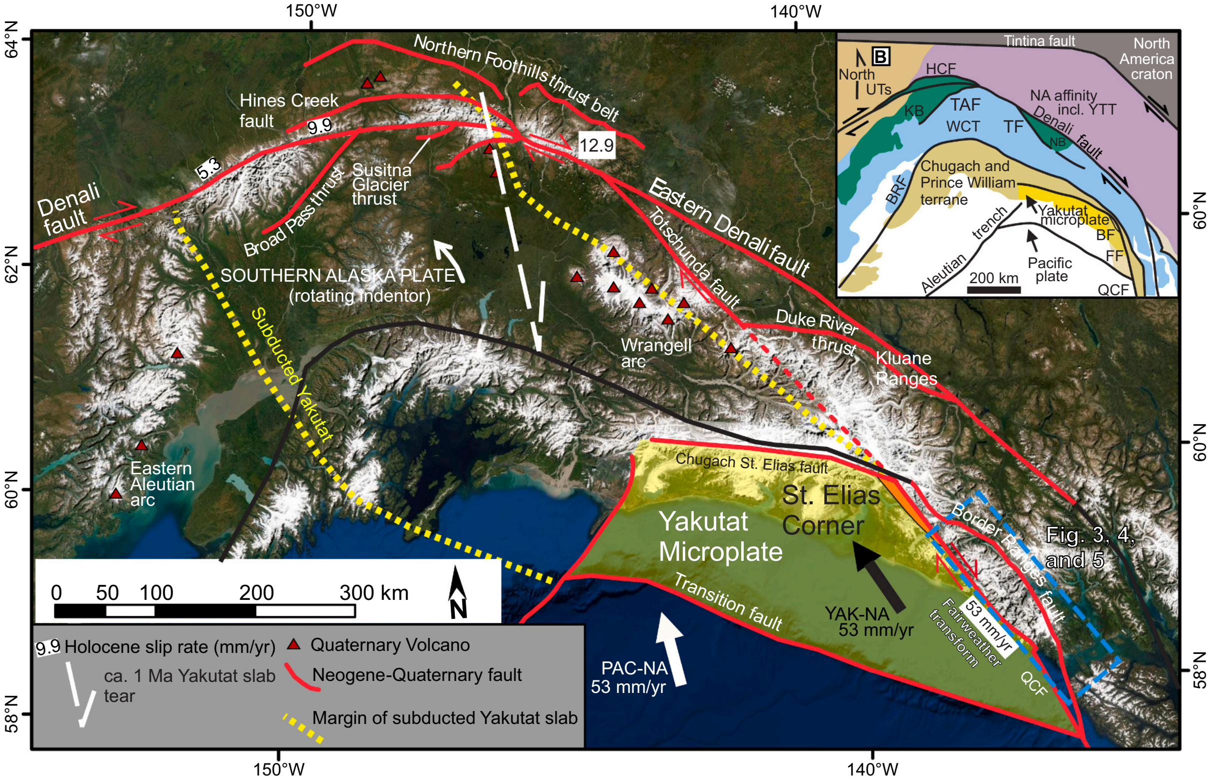

Fig. 1. (A) Digital globe satellite image of south-central Alaska showing the locations of Neogene-Quaternary fault systems discussed in the text, subducted and unsubducted portions of the Yakutat microplate (yellow) (Mann et al., 2022), Quaternary volcanoes (red triangles), orange polygon along northern Fairweather fault is the Boundary block, and approximate location of Figs. 3–5 (dashed blue box; Fig. 3 covers a larger footprint than the dashed blue box). Denali fault Holocene slip rates from Haeussler et al. (2008). Pacific-North America (PAC-NA) and Yakutat microplate-North America (YAK-NA) vectors from Elliott and Freymueller (2020). The margin of subducted Yakutat microplate is based chiefly on tomography and seismicity data (adapted from Mann et al., 2022). (B) The Inset in upper right shows the simplified terrane geology in the region of the satellite image. Abbreviations: FF—Fairweather fault, BF—Boundary fault, BRF—Border Ranges fault, HCF—Hines Creek Fault, KB—Kahiltna basin, QC—Queen Charlotte fault, TAF—Talkeetna fault, TF—Totschunda fault, UTs—unidentified terranes, NA—North America, YTT—Yukon-Tanana terrane, WCT—Wrangellia composite terrane. (For interpretation of the references to colour in this figure legend, the reader is referred to the web version of this article.)

Fig. 2. Photos of the Fairweather Range from the west (Pacific Ocean) and east (Glacier Bay). A) The Fairweather fault is the topographic break between the Fairweather welt and the Fairweather Range (Figs. 1 and 3). B) The Border Ranges fault is the eastern topographic break at the base of the Fairweather Range (Fig. 1B). Photos courtesy of the National Park Service.

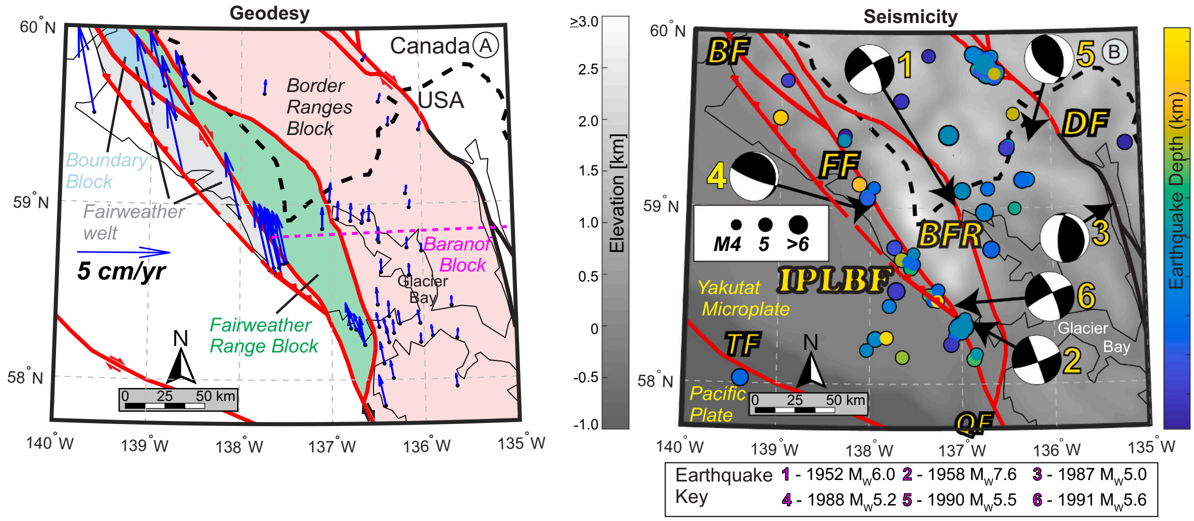

Fig. 3. (A) Post seismic and glacial isostatic corrected geodetic data (North American reference frame; Elliott and Freymueller, 2020) for our designated Fairweather welt (which includes the Boundary block), Fairweather Range block, and Border Ranges blocks. The Border Ranges block is moving distinctly differently (North-easterly) than the Fairweather Range block (Northernly). The magenta east-west dashed line is the original Baranof block boundary from Elliott and Freymueller (2020). (B) Earthquake data (>4 M; depth 0–30 km) from the complete USGS catalog (2001 to Present). The Fairweather block has experienced limited recorded seismicity. The Fairweather and Border Ranges faults indicate active seismic zones. See Table S1G and H for earthquake data and geodetic data details. Black dashed line USA-Canada border. Abbreviations: TF—Fairweather Fault, IPLBF—Icy Bay-Lituya Bay Fault, FF—Fairweather Fault, BF—Boundary Fault, BRF—Border Ranges Fault, DF—Denali Fault. (For interpretation of the references to colour in this figure legend, the reader is referred to the web version of this article.)

microplate, an oceanic plateau (Pavlis et al., 2004; Gulick et al., 2007; Worthington et al., 2012), from near Washington-Oregon since ca. 50 Ma (Wells et al., 2014; White et al., 2017). The ~280-km long Fairweather fault is linked to the ~850 km Queen Charlotte transform system to the south and together make up the north-east Pacific plate-North American plate boundary, as well as the modern north-east edge of the Yakutat microplate-North American plate boundary (e.g. Brothers et al., 2020) (Fig. 1).

It appears the Fairweather transform boundary is a younger component of the overall system, forming perhaps by 30 Ma (Plafker et al., 1994). The Fairweather transform boundary is localized on a single fault strand with a surface width of <100 m in places (Witter et al., 2021) and likely has been since formation (Ten Brink et al., 2018), similar to many long-lived highly oblique transform faults (e.g. Denali fault, <150 m wide; Benowitz et al., 2022a; Alpine fault, ~12 m wide; Barth et al., 2013). The Fairweather fault is also a lithospheric boundary with a complex history. To the east of the Fairweather fault, the Chugach terrane formed as an accretionary complex in the late Mesozoic and was subjected to low-pressure, high-grade metamorphism during a Paleocene-Eocene ridge-subduction event at a paleolatitude far south of its present position (e.g. Sisson and Pavlis, 1993; Pavlis and Sisson, 1995; Cowan, 2003; Gasser et al., 2011, 2012; Scharman et al., 2012). The Chugach terrane was displaced northward relative to the adjacent Wrangellia terrane by Paleocene-Eocene dextral re-activation of the Border Ranges fault with slip of at least 195 km and potentially >650 km (Roeske et al., 1992, 2003; Pavlis and Roeske, 2007).

The Yakutat microplate to the west of the Fairweather fault experienced an entirely different tectonic history than rocks to the east of the fault, the primary evidence for large-scale transport to its present position (Plafker et al., 1994) (Fig. 1). Specifically, seismic imaging (Worthington et al., 2012) and onshore geology (Chapman et al., 2012) show that the Yakutat microplate includes a remnant of a thrust-contact emplacing Chugach-like accretionary-complex rocks above underlying Eocene oceanic plateau rocks (Fig. 1B). This structural juxtaposition is interpreted as a remnant suture produced when the Yakutat oceanic plateau collided with the North American convergent margin in the Eocene (e.g. Worthington et al., 2012), prior to final transport northward along the Queen Charlotte-Fairweather transform system (Wells et al., 2014). The modern Queen Charlotte-Fairweather transform system follows the continent-oceanic plate boundary implying the unusual scenario of the oceanic plate being rheologically weaker than the neighboring continental plate (Ten Brink et al., 2018).

Along the northern transform boundary, the strike of the Queen Charlotte fault varies from N23°W offshore to the south, up to N47°W

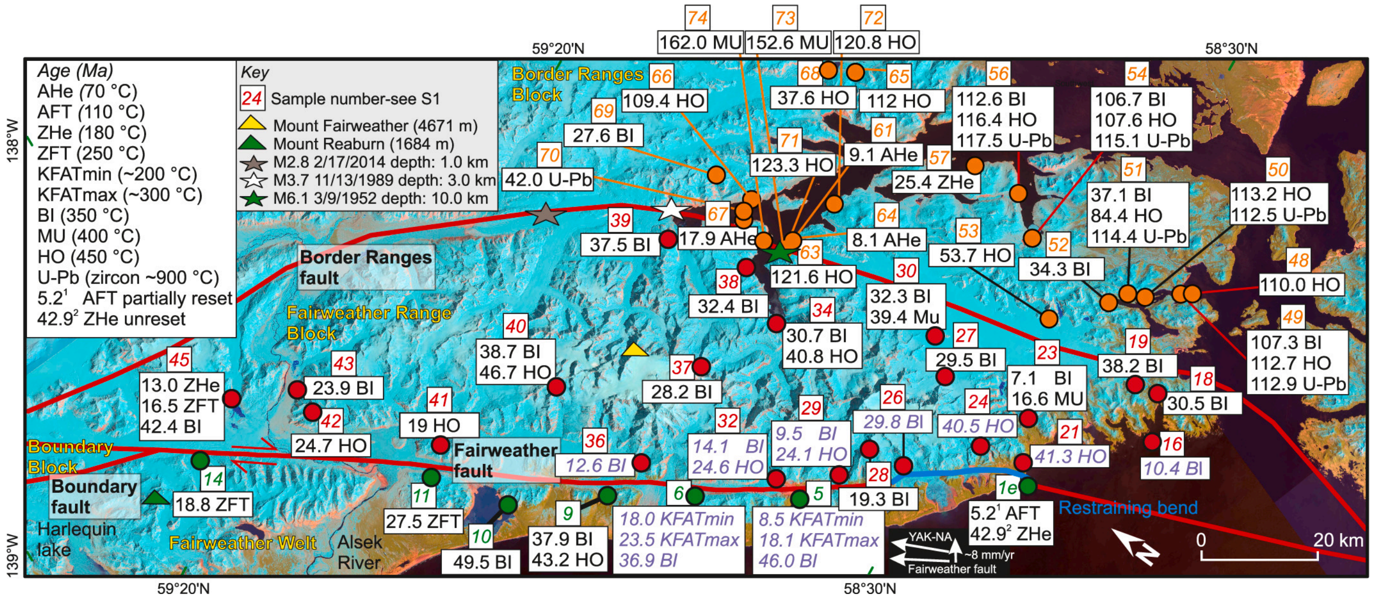

Fig. 4. Landsat images with sample locations and older than late Miocene ages (in Ma) from the Fairweather welt (ages in green), Fairweather Range block (ages in red), and the Border Ranges block (ages in orange). Select earthquakes along the Border Ranges fault shown. New data from this study are in purple and *italics*. Constraints for Yakutat-Fairweather fault convergence vector diagram at bottom right provided in the text. New and previously published data details are presented in Table S1E. (For interpretation of the references to colour in this figure legend, the reader is referred to the web version of this article.)

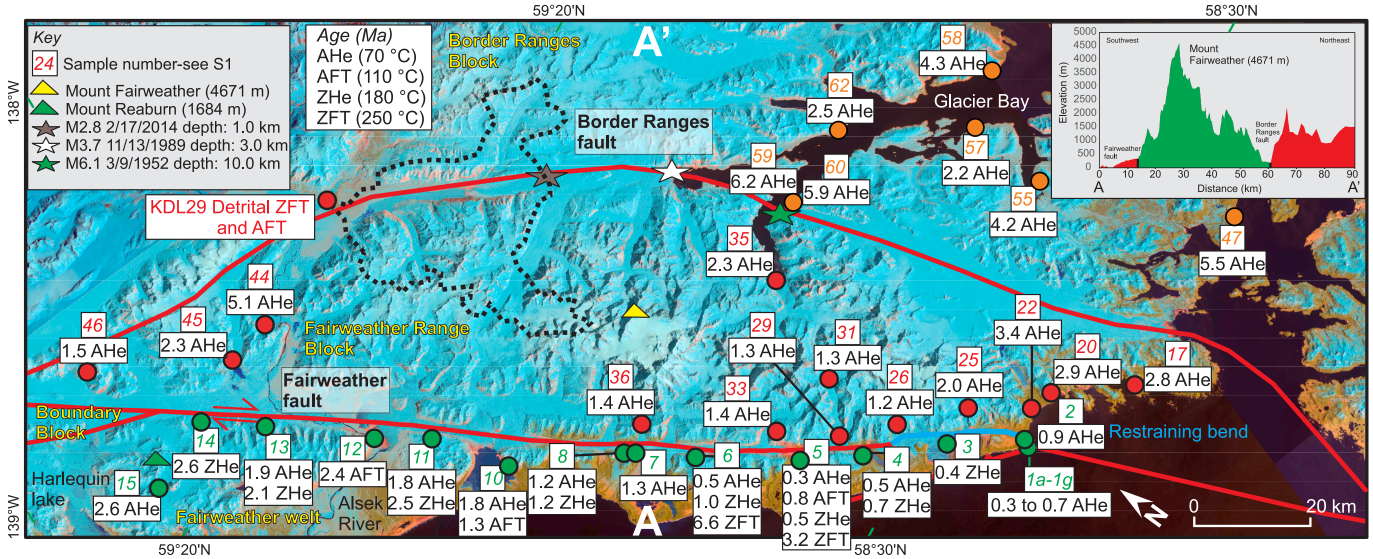

Fig. 5. Landsat images with sample locations and latest Miocene and younger ages (in Ma) from the Fairweather welt (ages in green), Fairweather Range block (ages in red), and the Border Ranges block (ages in orange). Select earthquakes along the Border Ranges fault shown. New and previously published data details are presented in Table S1E. Sample KDL29 is modern river sediment with a dotted line showing the approximate drainage watershed (Falkowski and Enkelmann, 2016). Topographic profile along A to A' in the upper right corner. (For interpretation of the references to colour in this figure legend, the reader is referred to the web version of this article.)

onshore along the Fairweather fault restraining bend, and approximately N33°W along the main Fairweather Range (Figs. 1 and 3). Estimates of the Fairweather fault horizontal and vertical slip rates are similar across different time scales. Elliott and Freymueller (2020) estimated a rate of 46 mm/yr from two decades of satellite geodesy data. Plafker et al. (1978) and Brothers et al. (2020) estimated a millennial slip rate based on offset geomorphic features of ~53 mm/kyr and Lease et al. (2021) estimated a million-year slip rate based on thermochronology analysis of 54 km/Myr (note: mm/yr = m/kyr = km/Myr, but reflect different spatiotemporal scales of measurements). The Fairweather fault geometry and modern Yakutat-NA vector yields a fault-perpendicular rate of ~9 mm/yr along the Fairweather restraining bend segment: similar to the geodetic modeled ~8 mm/yr convergence rate across the Fairweather fault (Elliott and Freymueller, 2020) which is a ~ 6:1 ratio of strike-slip to fault normal slip component. West of the Fairweather fault restraining bend there was a ~ 6 m:1 m ratio of horizontal-to-vertical slip distribution during the 1958 M7.8 earthquake (Tocher, 1960). The decadal scale based on GPS data (46.8 mm/yr; Elliott and Freymueller, 2020), millennial time frame based on geomorphic features (49/7 m/kyr Witter et al., 2018, 2021), and long-term time frame slip rates based on thermochronology analysis from the restraining bend (54/10 km/Myr; Lease et al., 2021) all have a generally similar ratio of horizontal-to-vertical slip rate distribution. However, the Fairweather fault restraining bend and associated reverse faults may be a relatively recent structural configuration with thermochronology analysis demonstrating its existence since at least ca. 2.6 Ma (Lease et al., 2021).

2.2. Yakutat oceanic plateau

The Yakutat microplate is a ~ 11–30 km thick oceanic plateau (e.g. Worthington et al., 2012). Flat-slab subduction of the Yakutat microplate under Alaska commenced by ca. 30 Ma (Plafker, 1987; Haeussler et al., 2008; Brueseke et al., 2019, 2023a) coeval or subsequent with the development of the Fairweather fault (Plafker et al., 1994). The modern dip of the subducted Yakutat slab is shallower to the west than to the east of a segmenting south-north-orientated slab tear (Fig. 1) (Mann et al., 2022). The Yakutat microplate also has south-to-north and west-to-east crustal thickness variations. The slab is thinnest inboard to the northwest (~11 km) and the thickest sector is mostly outboard and presently along the Fairweather transform boundary (~30 km) (Ferris et al., 2003; Rossi et al., 2006; Worthington et al., 2012; Pavlis et al., 2019; Mann et al., 2022).

The Yakutat microplate's convergence component with North America reflects the Pacific plate's relative motion changes through time (e.g., McAleer et al., 2009; Rosenthal et al., 2023). However, the modern Yakutat convergence angle with North America is N24°W, where the Pacific slab is converging at N15°W with North America (Elliott and Freymueller, 2020). Both slabs have generally the same convergence velocity of 53 mm/yr relative to North America (Elliott and Freymueller, 2020). It is unresolved when the Yakutat microplate underwent counterclockwise rotation and took on a different convergent angle than the unsubducted Pacific slab which has a larger surface area (~1200 X larger than the outboard unsubducted Yakutat slab).

2.3. Fairweather Range

There are large rock type contrasts across the Fairweather fault (Fig. 1B). Exposed rocks along the west side of the Fairweather fault, in our region of study, consist of Miocene-Pleistocene indurated and unconsolidated sedimentary cover strata, igneous intrusions, and low-grade metamorphic rocks (Wilson et al., 2015). The main igneous bodies east of the Fairweather restraining bend have U-Pb zircon emplacement ages ranging from ca. 49 to 39 Ma (Feldberg-Bannatyne et al., 2023). The Fairweather Range consists primarily of high-grade metamorphic rocks of the Chugach Terrane (Fig. 1B) with intrusive bodies that range from layered gabbro to granodiorite plutons of the Paleocene-Eocene Sanak-Baranof suite (Hudson et al., 1977a, 1977b; Wilson et al., 2015; Wackett et al., 2024). Igneous bodies east of the Border Ranges fault, dated with U-Pb zircon, have emplacement ages ranging from ca. 118 to 42 Ma suggesting different pulses of magmatism (e.g. Sisson et al., 2003; Holm-Denoma et al., 2020). Muscovite $^{40}Ar/^{39}Ar$ geochronology cooling ages are as old as ca. 162 Ma east of the Border Ranges fault (Roeske et al., 1992). The igneous bodies dated with U-Pb zircon geochronology, between the Fairweather and Border Ranges faults, have emplacement ages ranging from ca. 54 to 42 Ma (Sisson et al., 2003; Gasser et al., 2012; Falkowski et al., 2016; Feldberg-Bannatyne et al., 2023).

There are no known mapped faults between the Fairweather and the Border Ranges faults that can explain this region of high topography (McAleer et al., 2009). The Border Ranges fault has been assumed to be inactive as a major strike-slip fault in our region of interest since ca. 42 Ma on the basis of plutons that cross-cut the fault and are not offset along the Glacier Bay strand of the fault (Smart et al., 1996; Sisson et al., 2003). Nonetheless, the fault has low seismicity today, and elsewhere along the fault, cross-cutting relationships are contradictory due to multiple fault strands where younger faults bypass older fault segments with distinct cross-cutting relationships (Pavlis and Roeske, 2007). In the study area, the Border Ranges fault is a topographic break (Figs. 2, 3, and 5) suggesting this fault may be a long-lived active structure; a hypothesis we evaluate here.

Low-temperature apatite U-Th/He (AHe) cooling ages are older to the east of the Fairweather fault (youngest AHe; 1.2 Ma) compared to the west (youngest AHe; 0.3 Ma; Lease et al., 2021) (Fig. 4). Hence, the vast majority of Quaternary exhumation, and presumably Yakutat slab convergence, is taken up on the western side of the Fairweather fault restraining bend through exhumation (>6–8 mm/yr), but 1–2 Ma AHe cooling ages indicate Quaternary exhumation rates (0.7–1.7 mm/yr) in the Fairweather Range block (McAleer et al., 2009; Lease et al., 2021).

3. Methods

3.1. Fairweather Range regional geochronology compilation

For this study we compiled 109 published bedrock cooling ages from 75 Fairweather Range corridor samples (see Table S1F for detailed referencing) for the first time to examine the overall exhumation history of the Fairweather Range and the relation of the documented exhumation patterns to vertical extrusion between fault pairs (e.g. Fairweather and Border Ranges Faults) and to plate vector changes/micro-plate rotations. These published geochronology and thermochronology bedrock age results comprise: U-Pb zircon ages ($N = 6$), $^{40}Ar/^{39}Ar$ ages (hornblende [HO]: $N = 9$; muscovite [Mu]:$= 2$; biotite [BI]: $N = 7$), K-Ar ages (HO: $N = 9$; MU: $N = 2$; BI: $N = 14$), zircon fission track ages (ZFT: $N = 5$), zircon U-Th/He ages (ZHe: $N = 11$), apatite fission track ages (AFT: $N = 4$) and apatite U-Th/He ages (AHe: $N = 40$) bedrock datasets from 75 samples total (Figs. 4–7, and Table S1F). These data are complemented by one published modern river detrital ZFT-AFT data set (Figs. 5 and 8 and Table S1G) (Falkowski and Enkelmann, 2016) and 13 new $^{40}Ar/^{39}Ar$ geochronology ages from 9 samples, 5 on samples different than those with previous geochronology data, (Table S1A): (1) to better constrain patterns of rock cooling of the Fairweather Range nominally between 450 °C and 0 °C mean annual surface temperatures and (2) inferred exhumation patterns. (Harrison, 1982; Grove and Harrison, 1996; Lovera et al., 1997; Ketcham et al., 1999; Farley, 2000; Reiners et al., 2004; Bernet, 2009; Harrison et al., 2009; Historical Monthly and Derived Temperature Products, UAF SNAP, Fairbanks, Alaska).

3.2. New $^{40}Ar/^{39}Ar$ geochronology and thermochronology techniques

Four hornblende (HO), 7 biotite (BI), and 2 potassium feldspar (FS) mineral separates from 9 bedrock samples were analyzed using $^{40}Ar/^{39}Ar$ incremental step-heating experiments (Fig. 6). $^{40}Ar/^{39}Ar$ geochronology and thermochronology were performed at the University of Alaska Fairbanks Geochronology Facility. These samples were selected from the USGS Alaska sample archive based on availability, location in relation to the Fairweather fault, and lithology. Samples were crushed, sieved for the 250–1000 μm grain size, washed, and then separated using magnetic and handpicking mineral separation techniques. Samples were analyzed on a VG-3600 mass spectrometer using laser step-heating techniques described in Benowitz et al. (2014). A summary of all the $^{40}Ar/^{39}Ar$ results is given in Table S1A, with all ages quoted to $\pm 1\sigma$ and calculated using the decay constants of Renne et al. (2010). For a more detailed description of the $^{40}Ar/^{39}Ar$ analytical methods used and how uncertainties were derived, isotopic tables and figures see the Supplemental Materials (Text S1, Fig. S1, and Table S1A, B, C, and D).

The K-feldspar age spectra are interpreted using multi-domain diffusion modeling (Lovera et al., 1997) to understand their thermal histories. Instead of performing diffusion experiments, we look at the timing of closure of the high-temperature ($KFAT_{max}$: ~300 °C; K-feldspar argon thermochronology) and low-temperature ($KFAT_{min}$: ~200 °C) domains for K-feldspar (Lovera et al., 1997; Benowitz et al., 2014; Davids et al., 2018; Löbens et al., 2017).

Cooling curves are constructed for individual samples using the data

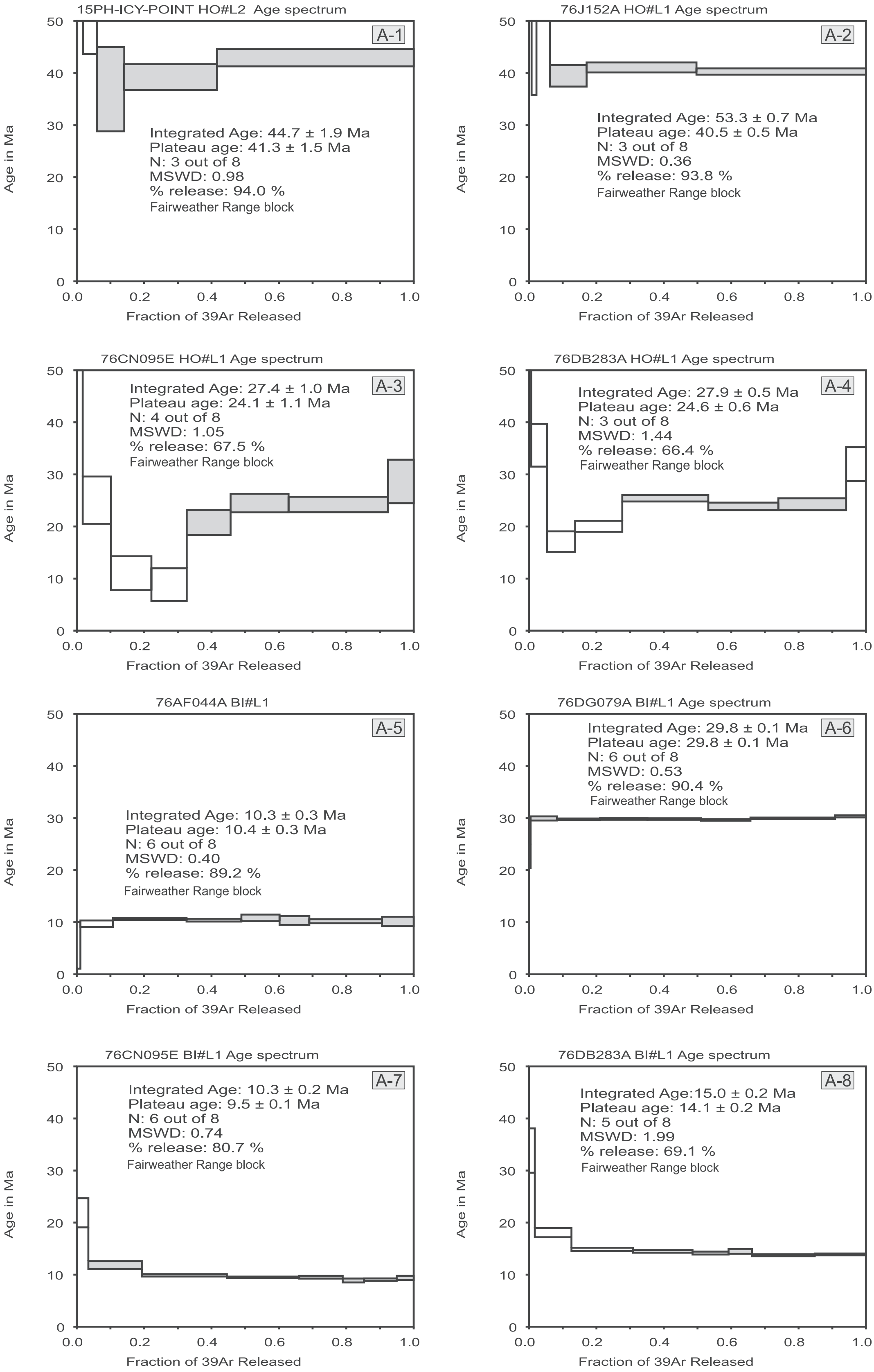

Fig. 6. (A) ^{40}Ar/^{39}Ar age spectra for new and previously published samples from the Fairweather welt, Fairweather Range block, and Border Ranges block. Grey boxes are the incremental heating steps chosen during age determination calculation. (B) Plateau age vs integrated age for the new ^{40}Ar/^{39}Ar hornblende and biotite ages. The blue line is the trend line. (C) Sample 16AWs001 from Wilson et al. (2021) and shown to demonstrate that Eocene-Oligocene hornblende and biotite ^{40}Ar/^{39}Ar and K-Ar ages east of the Border Ranges fault (Fig. 4) may be reflecting fully or partially resetting of older Cretaceous plutons from younger magmatic events. (For interpretation of the references to colour in this figure legend, the reader is referred to the web version of this article.)

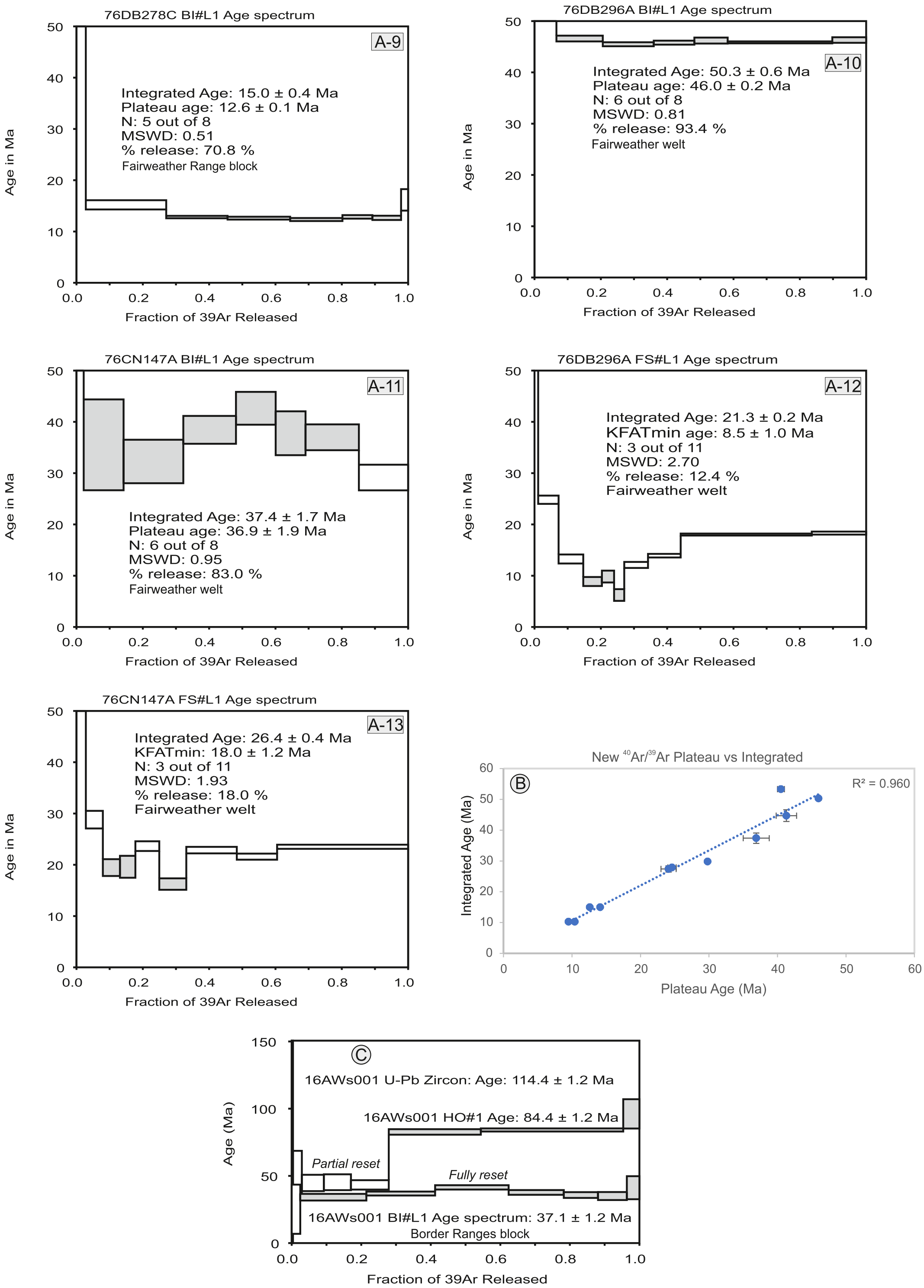

Fig. 6. (*continued*).

from a single sample or a composite of cooling ages from neighboring (<5 km) samples using nominal closure temperatures for each radiometric system (e.g. Reiners et al., 2005) (Table S1J, K and L). The cooling rate between time-temperature sample points is derived from the slope. Age probability function plots (e.g. histograms that take into account uncertainty) were constructed using Isoplot (Ludwig, 2012). We calculated simple plate vectors and fault displacement rates based on Pythagoras's theorem (e.g. Agarwal, 2020).

3.3. Seismic and vector analysis

Earthquakes greater than >M4 (U.S. Geological Survey ComCat earthquake catalog; January 2001 to January 2022) are plotted along with geodetic data (Elliott and Freymueller, 2020) from GPS stations in the study area, as well as major structural features (Fig. 3 and Table S1H and I) to investigate modern activity of faults bounding the Fairweather Range.

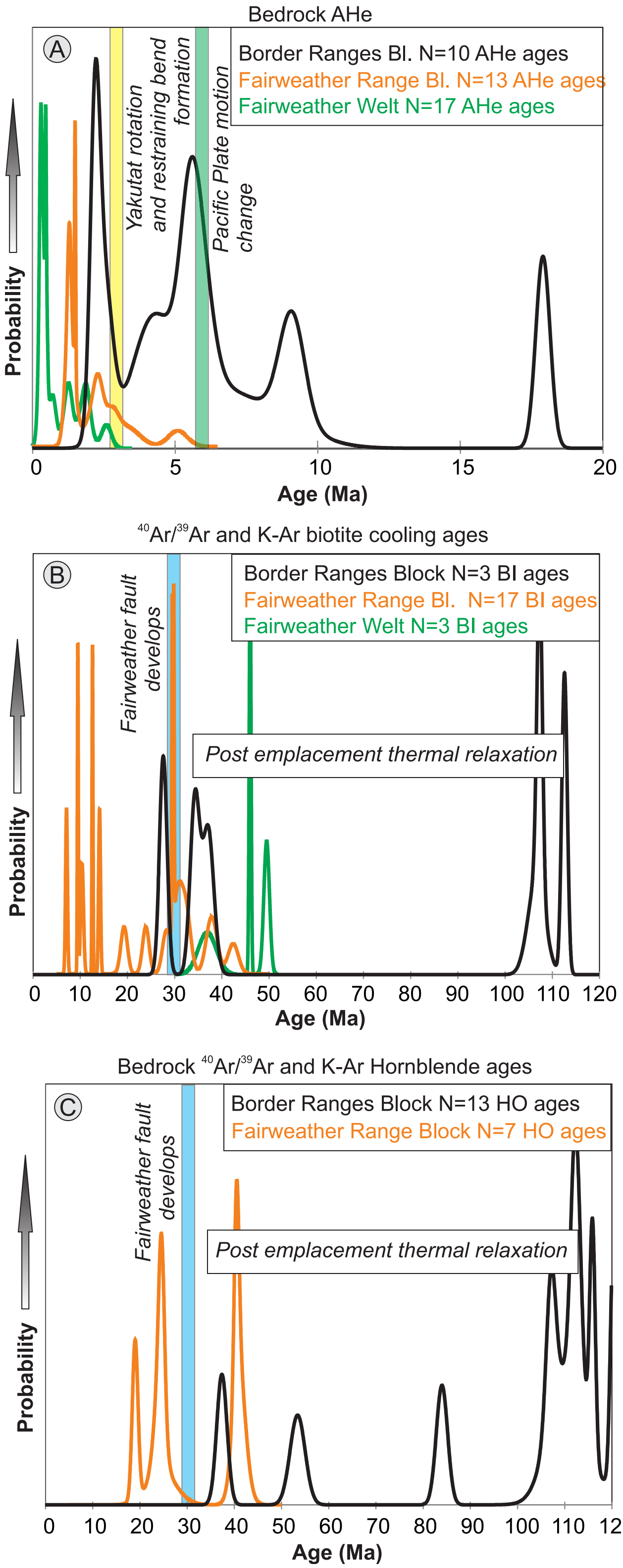

Fig. 7. Probability density function plots of bedrock geochronology and thermochronology data from the Fairweather welt, Fairweather Range block, and Border Ranges block. (A) AHe cooling ages. (B) ^{40}Ar/^{39}Ar and K-Ar biotite cooling ages. (C) Bedrock ^{40}Ar/^{39}Ar and K-Ar hornblende ages. Relevant tectonic events are shown with transparent bars. Data plotted are new and previously published (see Table S1E). Block is abbreviated for space as Bl.

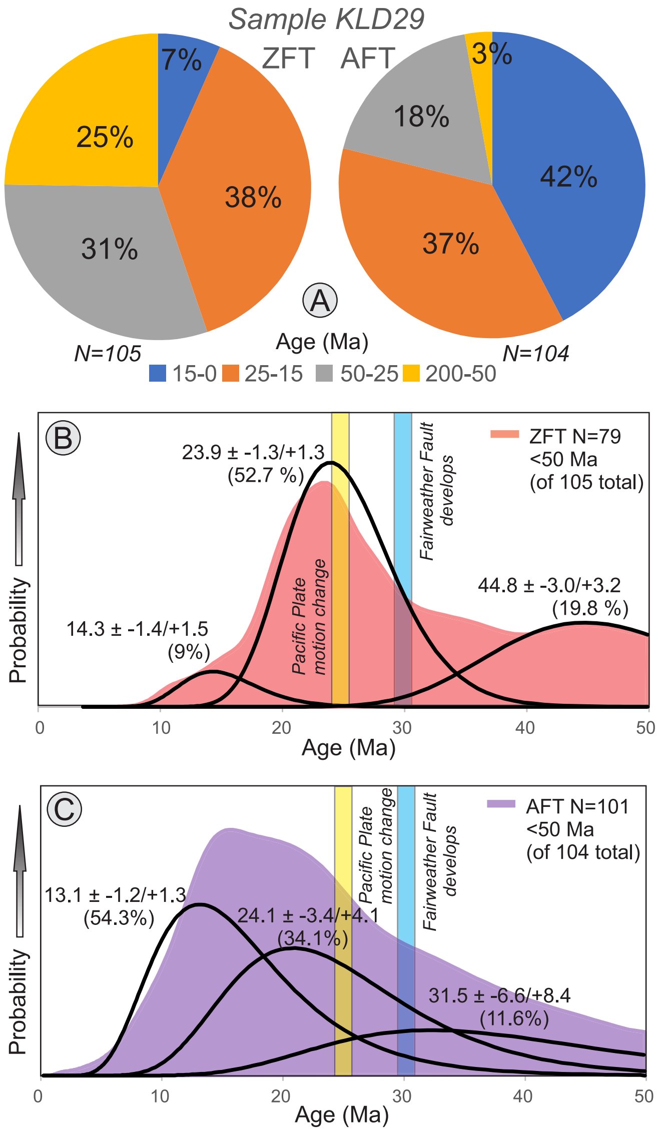

Fig. 8. (A) Pie graphs and (B-C) Binomial peaking fitting (Brandon, 1992, 1996) of detrital ZFT and AFT data from modern river sediment sample KDL29 (Table S1F) from Falkowski and Enkelmann (2016). Black lines are fitted peaks and the colored area are the total ZFT and AFT single grain age populations. Peak ages, asymmetric 1σ standard deviation, and the fraction of the total grains analyzed for each peak are shown. Single grain ages <50 Ma shown to highlight the time span of interest. Relevant tectonic events are shown with transparent bars. The location of this sample and approximate watershed is shown on Fig. 5.

4. Results

We divide, present, and discuss the geochronology, thermochronology, earthquake, and geodetic data by tectonic block. We define the Fairweather welt as the region between the outboard thrust front (e.g. Icy Point-Lituya Bay fault) and the Fairweather fault (Plafker, 1987; Bruhn et al., 2004) which is generally above sea level, the Fairweather Range block as the region between the Fairweather fault and the Border Ranges fault, and the Border Ranges block as the region east of the Border Ranges fault and west of the eastern Denali fault (Figs. 3–5). We define the Boundary block, which is part of the Fairweather welt, as the region between the Boundary and the Fairweather faults (Figs. 1, 3–5) (Schartman et al., 2019).

4.1. New ^{40}Ar/^{39}Ar geochronology and thermochronology results

4.1.1. Fairweather Range block

HO separates from samples 15PH-ICY-POINT (#21 Fig. 4), 76J152A (#24 Fig. 4), 76CN095E (#29 Fig. 4), and 76DB283A (#32 Fig. 4) of the Fairweather Range block region were analyzed for ^{40}Ar/^{39}Ar geochronology. The HO step-heat releases of samples (Fig. 6A-1) and #24 (Fig. 6A-2) had a generally flat age pattern indicative of minimal loss/alteration (e.g. Schaen et al., 2021). No isochron age determination was possible for these two samples because of the homogenous radiogenic content of the release. The HO step-heat releases of samples (Fig. 6A-3) and #32 (Fig. 6A-4) had a slightly stepping-up age pattern indicative of potential loss/alteration (e.g. Schaen et al., 2021). No isochron age determination was possible for these two samples because of the documented loss. Sample #21 had a plateau age of 41.3 ± 1.5 Ma, #24 provided a plateau age of 40.5 ± 0.5 Ma, #29 had a plateau age of 24.1 ± 1.1 Ma, and sample #32 provided a plateau age of 24.6 ± 0.6 Ma (Table S1A).

BI separates from samples 76AF044A (#16 Fig. 4), 76DG079A (#26 Fig. 4), 76CN095E (#29 Fig. 4), and 76DB283A (#32 Fig. 4), and 76DB278C BI#L1 (#36 Fig. 4) of the Fairweather Range block region were analyzed for ^{40}Ar/^{39}Ar geochronology. The BI step-heat releases of all of these samples had a generally flat age pattern (Fig. 6A5-9) indicative of minimal loss/alteration (Schaen et al., 2021). No isochron age determination was possible for samples #16, #32, and #36 because of the homogenous radiogenic content of the release. Isochron regressions to initial ^{40}Ar/^{36}Ar for samples #26 and #29 demonstrated no evidence of significant excess ^{40}Ar (#26: 296.1 ± 5.2; #29: 323.6 ± 12.6) (Fig. S1 and Table S1A). Sample #16 had a plateau age of 10.4 ± 0.3 Ma, #26, provided a plateau age of 29.8 ± 0.1, Ma, #29 had a plateau age of 9.5 ± 0.1 Ma, #32 had a plateau age of 14.1 ± 0.2 Ma, and sample #36 provided a plateau age of 12.6 ± 0.1 Ma (Table S1A).

4.1.2. Fairweather welt

BI and FS separates from sample 76DB296A (#5 Fig. 4) and sample 76CN147A (#6 Fig. 4) of the Fairweather welt region were analyzed for ^{40}Ar/^{39}Ar geochronology. The step-heat releases of the BI separates had a generally flat age pattern (Fig. 6A10-11) indicative of minimal loss/alteration (Schaen et al., 2021). Sample #5 had a plateau age of 46.0 ± 0.2 Ma and sample #6 provided a plateau age of 36.9 ± 1.9 Ma (Table S1A). Isochron regressions to initial ^{40}Ar/^{36}Ar (#5: 293.6 ± 2.2; #6: 290.9 ± 5.6) demonstrated no evidence of excess ^{40}Ar (Fig. S1 and Table S1A).

FS step heating results from samples #5 and #6 had down-stepping age patterns potentially reflective of prolonged cooling (Fig. 6A12-13) (Lovera et al., 1997). Sample #5 had a 3 step minimum age (12% of ^{39}Ar release) of 8.5 ± 1.0 Ma with an imprecise regression to initial ^{40}Ar/^{36}Ar of 332.7 ± 59.6 (Fig. S1 and Table S1A). Sample #6 had a 3 step minimum age (18% of ^{39}Ar release) of 18.0 ± 1.2 Ma with an imprecise regression to initial ^{40}Ar/^{36}Ar of 403.5 ± 79.2 (Fig. S1 and Table S1A).

4.2. Published and new geochronology and thermochronology compiled results

In our following descriptions, we generally refer to K-Ar and ^{40}Ar/^{39}Ar ages simply by the mineral phase date to be succinct. New results (Fig. 6) and compilations of new and previously published data are shown on Figs. 4, 5, 7–10 (O'Sullivan et al., 1997; Sisson et al., 2003; McAleer et al., 2009; Brew et al., 2014; Falkowski and Enkelmann, 2016; Falkowski et al., 2016; Holm-Denoma et al., 2020; Lease et al., 2021; Wilson et al., 2015, 2021; this study). See Table S1F for detailed results and detailed data set referencing.

4.2.1. Fairweather Range block

HO ages range from ca. 46.1 Ma to 19.0 Ma. MU ages range from ca. 39.4 to 16.6 Ma (Fig. 4). BI ages range from ca. 42.4 to 7.1 Ma. A single ZFT age is ca. 16.5 Ma. A single ZHe age is ca. 13.0 Ma. AHe ages range from ca. 5.5 to 1.4 Ma. HO, BI, and AHe cooling ages trend towards younger from east to west, towards the Fairweather fault (Fig. 9 and Table S1M). ZFT and AFT single grain age data from a previously collected modern river (Alsek) sediment sample (KLD29) (Figs. 3 and 8) are mainly sourced from the Fairweather Range block (Falkowski and Enkelmann, 2016). Detrital ZFT cooling ages are primarily early Miocene (~38%) and detrital AFT cooling ages are primarily late Miocene (~42%) (Fig. 8A) in these modern river sediments. HO, BI, and AHe cooling ages are either not correlated with elevation or inversely correlated (Fig. 11 and Table S1N). MU ($N = 2$), ZFT ($N = 1$), and ZHe ($N = 1$) are not plotted due to limited numbers.

4.2.2. Fairweather welt

A single HO age is ca. 43.2 Ma. BI ages range from ca. 49.5 to 36.5 Ma. KFATmax ages range from ca. 23.5 Ma to 18.1 Ma and KFATmin ages range from ca. 18.0 to 8.5 Ma. ZFT ages range from ca. 27.5 Ma to the north to ca. 3.2 Ma to the south. ZHe ages range from ca. 2.6 Ma to the north to ca. 0.4 Ma to the south. AFT ages range from ca. 2.4 Ma to the north to ca. 0.8 Ma to the south. AHe ages range from ca. 2.6 Ma to the north to ca. 0.3 Ma to the south. Unreset sedimentary unit ZHe (42.9 Ma) and AFT (5.2 Ma) ages are shown on Fig. 4, for sample 1e. ZHe and AHe cooling ages are not correlated with elevation (Fig. 11 and Table S1N). HO ($N = 1$), BI ($N = 4$), ZFT ($N = 4$), KFAT ($N = 2$), and AFT

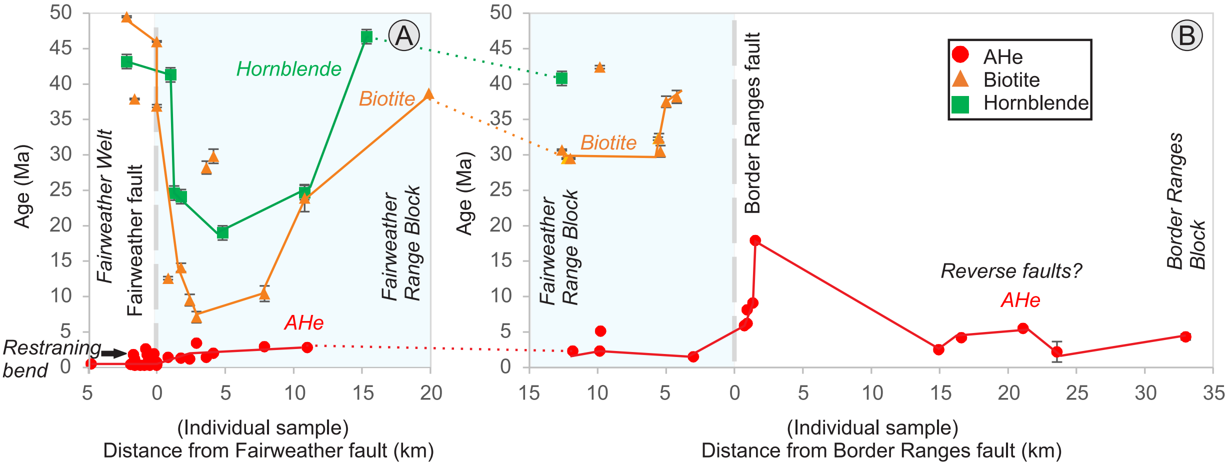

Fig. 9. Distance towards the Fairweather (A) and Border Ranges (B) faults for each individual sample shown on Figs. 4 and 5 and Table S1L. Faults shown are reference frame distances from individual samples not actual location-strike of the faults. Sample #15 is not plotted for scaling optimization.

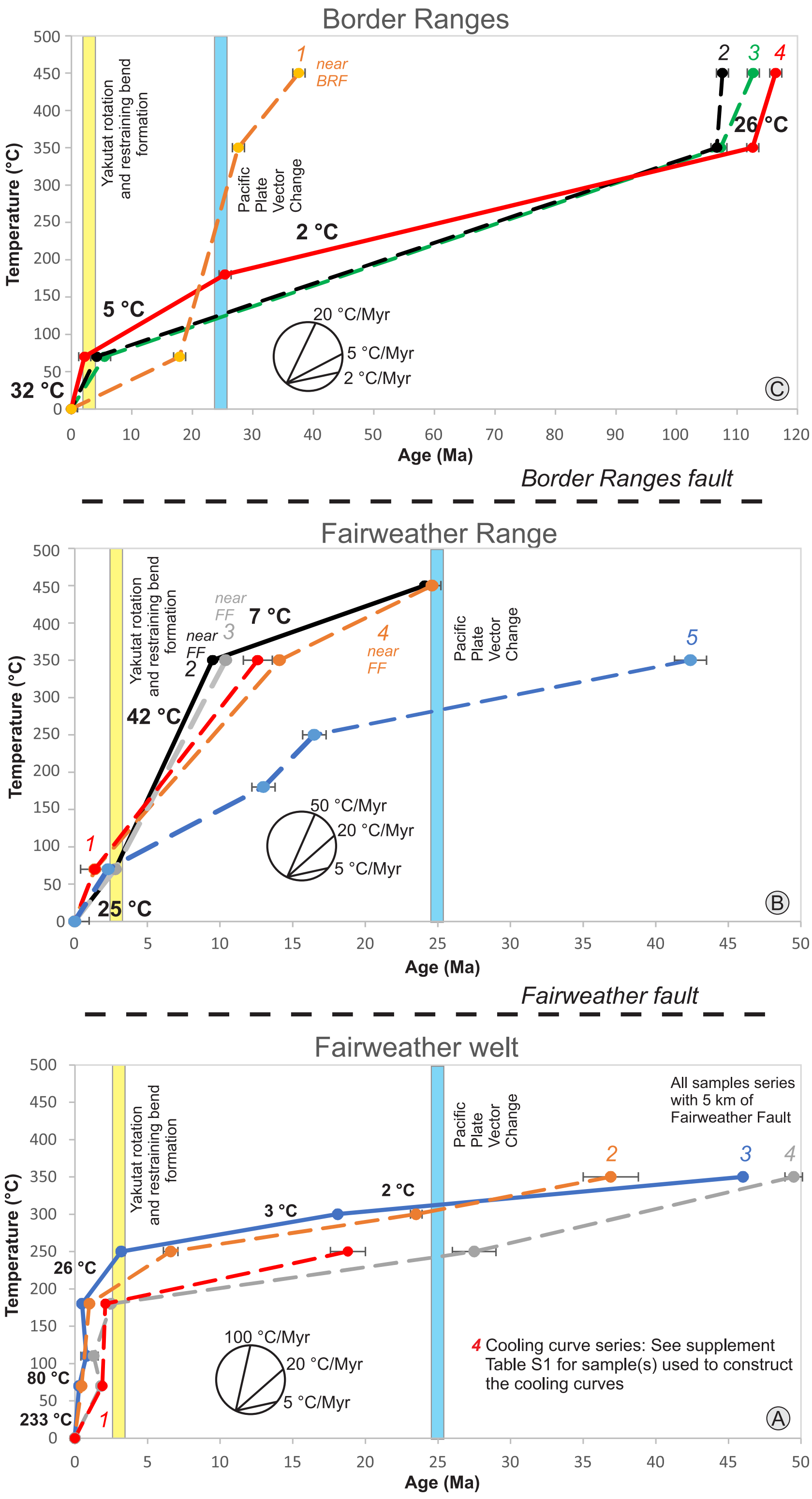

Fig. 10. Cooling curves (dashed and solid lines) based on nominal closure temperatures for different mineral systems from intrasample and near-by (~1 km) samples from the Fairweather welt, Fairweather Range block, and Border Ranges block. Solid lines are representative cooling curves with averaged cooling rates presented (°C = °C/Myr). See Table S1I, J, and K for details of which samples are used for each individual cooling curve-keyed to the series number on the figure. Blue bar highlights the ca. 25 Pacific plate vector change (Jicha et al., 2018) and the Yellow bar highlights the inferred ca. 3 Ma Yakutat microplate rotation (this study). Circles have angle of representative rock cooling trajectories and associated time-average cooling rates for each plot. Samples <~5 km from the Fairweather or Border Range fault noted. FF—Fairweather fault, BRF—Border Ranges fault. (For interpretation of the references to colour in this figure legend, the reader is referred to the web version of this article.)

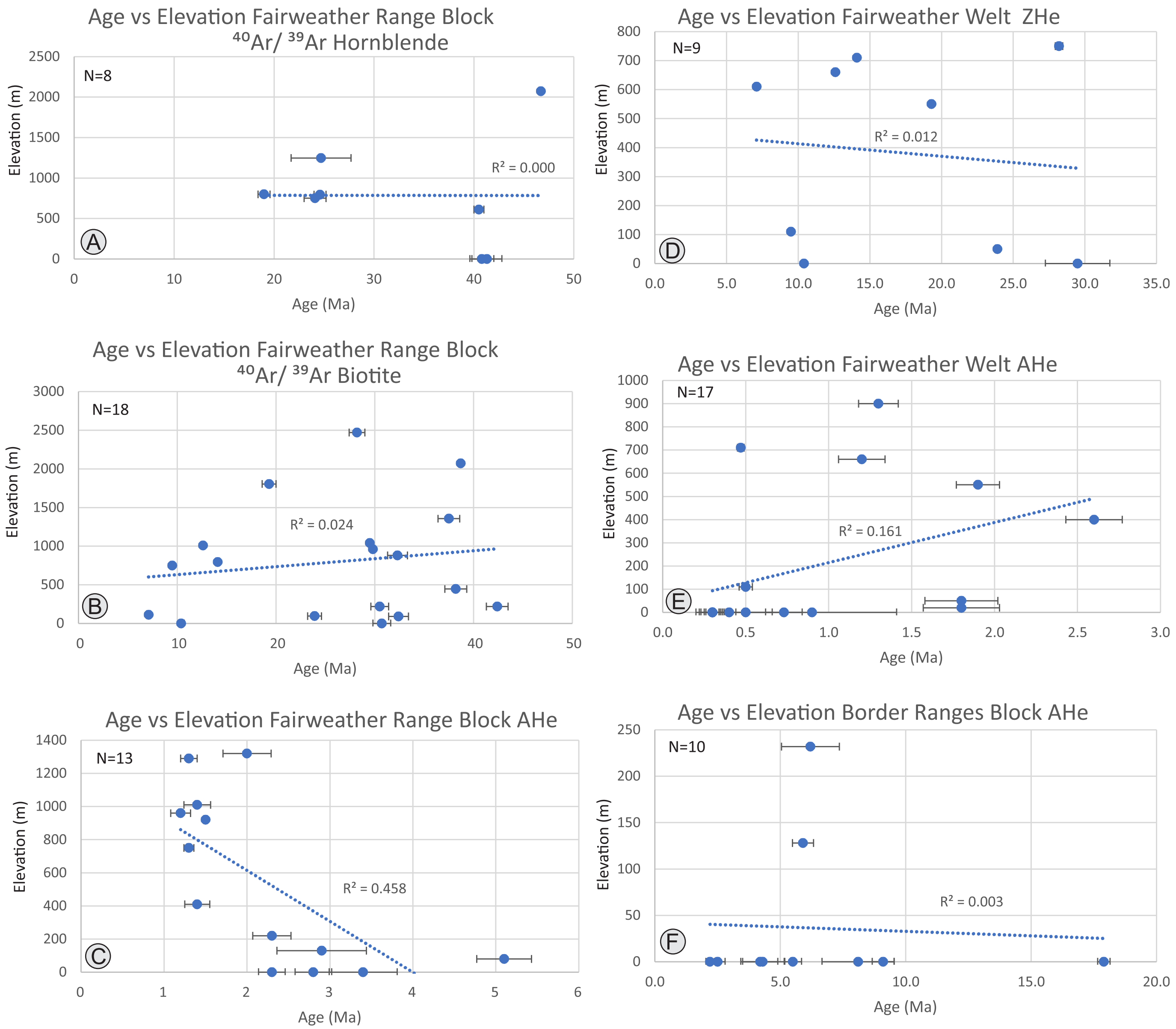

Fig. 11. Elevation vs age plots for (A) Fairweather Range block ^{40}Ar/^{39}Ar hornblende, (B) Fairweather Range block ^{40}Ar/^{39}Ar biotite, (C) Fairweather Range block AHe, (D) Fairweather welt ZHe, (E) Fairweather welt ^{40}Ar/^{39}Ar AHe, and (F) Border Ranges block AHe. There is no positive age correlation with elevation as expected for simple block uplift (Fitzgerald and Malusà, 2019). Radiometric systems for each block that had a limited number (<5) of cooling ages were not plotted.

(N = 4) were not plotted due to the limited number of samples.

4.2.3. Border Ranges block

HO ages range from ca. 121.6 to 37.6 Ma. BI ages range from ca. 112.6 to 27.6 Ma. ZHe ages range from ca. 25.4 to 13.0 Ma. AHe ages range from ca. 17.9 to 2.2 Ma. AHe cooling ages trend younger at greater distances from the Border Ranges fault to the east. AHe cooling ages are not correlated with elevation (Fig. 11 and Table S1N). HO and BI were not plotted because they reflect post emplacement thermal relaxation (discussed below). ZHe (N = 2) were not plotted due to the limited number of samples.

4.3. Fairweather Range region seismicity and geodetic data patterns

Published USGS earthquake and geodetic data (Elliott and Freymueller, 2020) are plotted in Fig. 3 and presented in Table S1H and I. These data are not adjusted in any way from their original sources. There is limited seismicity (>4 M; depth 0–30 km) between the Fairweather fault and the Border Ranges fault within the Fairweather Range block (Fig. 3). There are numerous recorded earthquakes along the east side of the Fairweather fault, along and west of the Border Ranges fault, and within the Yakutat microplate (Figs. 3 and 4). Geodetic data from the Fairweather Range block and Fairweather welt (Elliott and Freymueller, 2020) have generally north-west directed motion (Fig. 3). Geodetic data from the Border Ranges block have north-east directed motion.

5. Discussion

5.1. New ^{40}Ar/^{39}Ar hornblende and biotite ages quality

Overall the new ^{40}Ar/^{39}Ar HO and BI ages indicate minimum Ar loss due to alteration based on a strong correlation between plateau and integrated ages ($R^2 = 0.960$) (Figs. 6b and S1E). However, age spectra from BI have been shown to be a potentially unreliable means to evaluate Ar concentration gradients because of possible instability during heating in vacuo (Gaber et al., 1988). We choose to use the plateau age for our BI (and HO) results for comparison to previously published data, but acknowledge with the limited number of incremental heating steps (8) we may have missed some attributes of the Ar concentration gradients for these mineral separates. Our new ^{40}Ar/^{39}Ar HO and BI ages are similar to ^{40}Ar/^{39}Ar and K-Ar data from nearby samples with previously published ^{40}Ar/^{39}Ar and K-Ar data (Fig. 4) and are concordant with other radiometric systems from the same or nearby samples (Fig. 10). Hence, we have confidence in our new ^{40}Ar/^{39}Ar HO and BI age results and interpretations even with limited incremental heating step analysis.

5.2. Resetting

162–152 Ma ^{40}Ar/^{39}Ar muscovite cooling ages from trondhjemite bodies (Roeske et al., 1992; Smart et al., 1996) indicate the presence of Jurassic igneous bodies east of the Border Ranges fault (Fig. 4). ^{40}Ar/^{39}Ar HO ages are as old as ca. 123 Ma implying likely magmatism around this time (Fig. 4). U-Pb ages from the Border Ranges block range from 117.5 to 42.0 Ma (Sisson et al., 2003; Holm-Denoma et al., 2020). However partially reset ^{40}Ar/^{39}Ar HO (ca. 84.4) and fully reset ^{40}Ar/^{39}Ar BI (ca. 37.1 Ma) cooling ages from sample 51 (16AWs001, U-Pb zircon ca, 114.4 Ma, #51 Figs. 4 and 6) indicate the likely presence of late Eocene-Oligocene magmatism east of the Border Ranges fault. Hence HO and BI cooling ages from the Border Ranges block are not discussed in detail here because there is insufficient data to fully evaluate the level of resetting. Nonetheless, we infer these older high-temperature thermochronology data align with results from north of the St. Elias convergent corner, (Fig. 1) where ZFT cooling ages increase dramatically to the north across the Border Ranges fault indicating shallower Neogene exhumation inboard of this structure (Enkelmann et al., 2008; Enkelmann et al., 2015b).

5.3. Age patterns and cooling paths

Overall, there is no positive correlation between cooling ages (for each radiometric system) and elevation indicating possible structural control on cooling age patterns (Figs. 4, 5, 9, and 11) as documented along other major strike-slip fault systems (Benowitz et al., 2011; Niemi et al., 2013). Cooling curves constructed using nominal 'closure' temperatures for each radiometric system are all concordant (Figs. 10 and S1J, K and L), except the lower closure temperature window for FS (~200 °C) (Lovera et al., 1997; Wong et al., 2023) which is discordant with the ZFT (~250 °C) (Reiners and Brandon, 2006; Bernet, 2009) results. We have no way to determine why these FS and ZFT data are slightly discordant, but acknowledge the application of nominal closure temperatures can only approximate true closure temperatures. These assigned closure temperatures do not take into account the intrinsic qualities of each sample/crystal (e.g. chemistry, radiation damage, grain size, etc.) that may be affecting true closure temperatures (e.g. Reiners and Brandon, 2006). Furthermore, these $\mathrm{KFAT_{min}}$ age results are older than ZFT ages from the same sample and may be reflecting unaccountable excess ^{40}Ar. Hence we do not plot nor further consider these $\mathrm{KFAT_{min}}$ minimum age results.

5.3.1. Fairweather Range block

A compilation of all HO and BI ages from the Fairweather Range block shows the largest probability peak is at ca. 40 Ma for HO and at ca. 30 Ma for BI (Fig. 7). This gap in cooling ages (ca. 10 Ma) and associated closure temperatures (450 to 350 °C; e.g. Reiners et al., 2005) suggests strongly the BI ages are reflecting exhumation related cooling, not thermal relaxation from pluton emplacement cooling which would involve more rapid cooling rates (to ambient crustal temperatures in ca. 1 Ma; Nabelek et al., 2012). Detrital ZFT (~250 °C; Reiners and Brandon, 2006; Bernet, 2009) and AFT (~110 °C; Ketcham et al., 1999) have a lower nominal closure temperature than Ar BI (~350 °C; Grove and Harrison, 1996). Previously published detrital ZFT ages (Falkowski and Enkelmann, 2016), sourced primarily from the Fairweather Range block, show a binomfit extracted (Brandon, 1992, 1996) large peak population (~53%) of single grain ages at ca. 24 Ma. (Figs. 5 and 8B). Detrital AFT ages from the same study have a large peak population (~54%) of single grain ages at ca. 13 Ma (Falkowski and Enkelmann, 2016) (Figs. 5 and 8B). The suggested minimum age for the initiation of the Fairweather transform boundary (Plafker et al., 1994) by ca. 30 Ma is supported by these temperature-concordant BI (ca. 30 Ma), ZFT (ca. 24 Ma) and AFT (ca. 13 Ma) cooling age populations. However, it is likely the Fairweather fault or an equivalent transform boundary existed from ca. 50 to 30 Ma to facilitate the translation of the Yakutat microplate from its formation area near present day Washington-Oregon (Haeussler et al., 2008; Wells et al., 2014) north to the Wrangell trench south of the Wrangell arc (Fig. 1) by ca. 30 Ma (Berkelhammer et al., 2019; Brueseke et al., 2019; Trop et al., 2022).

If there was a pre-30 Ma transform boundary and associated sliver outboard of the Fairweather fault, the fault-bound block would have been translated into the St. Elias convergent corner (Fig. 1) with the initiation of the Fairweather fault as the new plate boundary. Speculatively, we suggest the Boundary block, delineated by the Boundary and Fairweather faults, and located near the terminus of the Fairweather fault system (Figs. 1, 3–5) may be such a remnant feature given similar Chugach terrane rock types in the Fairweather Range block, but with a distinctly different metamorphic history that is both older than and at higher pressures than, the adjacent Fairweather block (Sisson et al., 2003) as well as showing a distinct low-temperature thermochronology cooling history (see Schartman et al., 2019). Alternatively, a hypothetical paleo-transform boundary/sliver has fully subducted down the Wrangell (i.e. eastern Aleutian trench) trench.

Cooling age patterns are known to vary across and towards active structures (Spotila et al., 2007a). HO, BI, and AHe ages of the Fairweather Range block generally get younger towards the Fairweather fault (Fig. 9 and Schartman et al., 2019). There currently is not enough proximal high temperature data from the Fairweather Range block to evaluate if cooling ages get younger towards the Border Ranges fault (Fig. 9). Rapid cooling commenced for this block by ca. 25 Ma (7–10 °C/Myr), became rapid in late Miocene time (22–42 °C/Myr), and remained rapid after ca. 3 Ma (25–50 °C/Myr) (Fig. 10 and Table S1L). We suggest the late Oligocene increase in cooling rates in the Fairweather Range maybe linked with the ca. 25 Ma Pacific plate motion change that involved a ~ 12° counter-clockwise change (Doubrovine and Tarduno, 2008-plate circuit reconstruction; Jicha et al., 2018-multiple hot spots) and a 53% increase in the Pacific-Yakutat relative plate motion velocity (Jicha et al., 2018). This Pacific plate motion change is documented along four Pacific Basin seamount chains (Jicha et al., 2018) with associated deformation events along circum-Pacific faults (Denali- Trop et al., 2019; Fairweather-this study; Alpine Fault- Kamp, 1991; Batt et al., 2004; San Andreas- Sharman et al., 2013).

Cooling rates are time averaged from ca. 14–10 Ma to 3–1 Ma (Fig. 5), but we infer that the late Miocene graphical inflection towards more rapid cooling rates for the Fairweather Range block occurred at ca. 6 Ma as seen elsewhere in Alaska (Waldien et al., 2018; Benowitz et al., 2022a, 2022b; Rosenthal et al., 2023). We suggest this late Miocene increase in cooling rates may be related to the ca. 6 Ma relative Pacific-Yakutat plate motion change to more orthogonal (~13 to 18° clockwise rotation) that produced greater across fault convergence along the Fairweather fault at this time (Engebretson et al., 1985; Bruhn et al., 2004; Doubrovine and Tarduno, 2008; Austermann et al., 2011; Choi et al., 2021). These overall cooling age patterns of younger cooling ages, for all radiometric systems, as one approaches the Fairweather fault from the east (Figs. 4, 5, and 9) support possible differential exhumation and east-west tilting of the Fairweather block since at least ca. 25 Ma.

5.3.2. Fairweather welt

It is difficult to fully determine the pre-3 Ma cooling history of the Fairweather welt because material is being translated to the northwest at ~50 km/Myr into the St. Elias convergent corner (Fig. 1) which is a different tectonic and climatic environment than the one investigated here (Enkelmann et al., 2015b; Schartman et al., 2019). Their results from the Boundary block indicate rapid cooling after ca. 5 Ma and before 2 Ma with rates of 80–120 °C/Myr and inferred exhumation rates of ~3–6 km/Myr (assuming a geothermal gradient of 25 ± 5 °C/km). However, these rapid latest Pliocene ~3–6 km/Myr exhumation rates for the Boundary block (Figs. 1 and 3) followed by 1 km/Myr since 2 Ma (see Schartman et al., 2019), may in part reflect the block's leading edge late Pliocene position within the developing restraining bend before northward translation. HO and BI cooling ages from the southeast St. Elias convergent corner are generally older than Oligocene (Wilson et al., 2015; Falkowski et al., 2016) and ZHe cooling ages are generally early Miocene or older (Schartman et al., 2019). Limited BI ($N = 3$) ages from the Fairweather welt (Figs. 3, 6, and 7) in our study area have ca. 50 Ma ages similar to the known age of plutons in the region (Feldberg-Bannatyne et al., 2023).

These geochronological data sets imply overall slow pre-3 Ma rock cooling rates for the southeastern Fairweather welt (Figs. 1 and 3). Cooling rates pick up in the latest Miocene (13 °C/Myr) and after ca. 3 Ma cooling rates are rapid (40–233 °C/Myr) punctuated by a short-lived pulse of extreme cooling when rocks are transported through the restraining bend (Fig. 10 and S1J) (Lease et al., 2021). AHe cooling ages from the Fairweather welt get younger within the Fairweather fault restraining bend, but there has not been deep Neogene exhumation similar to the Fairweather Range block due to the material being rapidly advected through the Fairweather restraining bend.

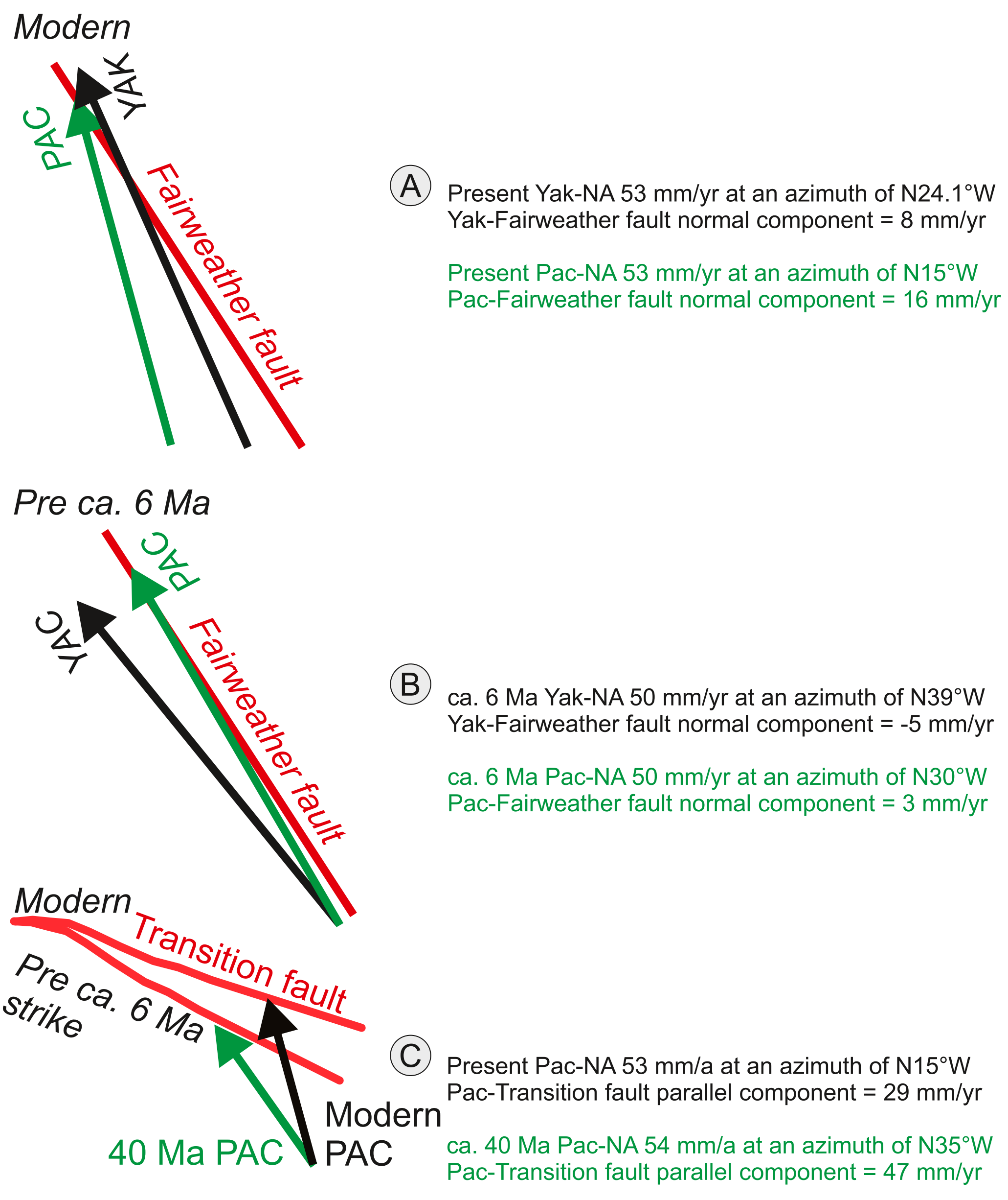

Fig. 12. Vector component analysis of the modern (A) Yakutat and Pacific slab vectors (Elliott and Freymueller, 2020) and (B) With 15° counter-clockwise rotation to pre-6 Ma plate vectors (Doubrovine and Tarduno, 2008). The Yakutat slab would not have a fault normal component (−6 mm/yr) in relation to the Fairweather fault (N33°W strike north of the restraining bend) when rotated back from the slab's present relative orientation with North America to pre-6 Ma plate vectors. Hence, we infer that a 9° counter-clockwise plate-motion rotation of the Yakutat slab occurred since 6 Ma synchronous with the counter-clockwise rotation of the Yakutat slab. (C) The Transition fault (N18°W strike) is currently not orientated in relation to the modern Pacific slab vector to accommodate significant strike-slip motion and be a transform boundary. If the Yakutat slab/Transition fault is rotated 9° clockwise to pre-6 Ma orientation, under the ca. 40 Ma to 35 Ma Pacific vector (N35°W Doubrovine and Tarduno, 2008), then the structure may have been a transform boundary.

5.3.3. Border Ranges block

Within the Border Ranges block AHe cooling ages are youngest away from the Border Ranges fault (McAleer et al., 2009) (Fig. 9 and Table S1M). This type of cooling age pattern is common when distal structures from the main strand are regions of focused exhumation (Spotila et al., 2007b). Cooling rates are generally slow for the Border Ranges block (2–4 °C/Myr) until after ca. 3 Ma when cooling rates increase dramatically (>32 °C/Myr) (Fig. 10 and Table S1L). We infer there are structures east of the Border Ranges fault that are playing a role in the late Pliocene-Quaternary rapid exhumation of this region supported by seismicity patterns (Fig. 3), but these structures remain relatively cryptic.

5.4. Relative plate motion and vector analysis

We performed a simple vector analysis to examine the paleo-motion vectors of the Pacific and Yakutat slabs before the ca. 6 Ma Pacific-Yakutat plate motion change (~13 to 18° clockwise rotation, 6–37% increase in North America convergence rates) (Engebretson et al., 1985; Doubrovine and Tarduno, 2008; Austermann et al., 2011) (Fig. 12) in the framework of the rock cooling history for the Fairweather welt, Fairweather Range block and Border Ranges block (Figs. 7, 9, and 10). The pre-6 Ma plate vector of the Pacific plate (N30°W) aligns better with the present day Fairweather fault's strike (strike of N33°W) and the pre-6 Ma transpressive history (~3 mm/yr fault normal component). However, a conjectural pre-6 Ma Yakutat microplate paleo-vector (assuming the 9° modern difference between the plates applies) of (~N39°W) does not (negative ~5 mm/yr fault normal component) align with either the strike of the Fairweather fault or the regions pre-6 Ma transpressive history (Fig. 12). Hence, we infer the Yakutat microplate experienced a 9° counter-clockwise plate motion change after ca. 6 Ma.

Furthermore, the Transition fault (Fig. 1), the high-angle fault boundary that bounds the Yakutat microplate to the southwest (e.g. Christeson et al., 2010) may have been a major strike-slip fault before 30 Ma that was involved with the northward translation of an inferred missing piece of the Yakutat microplate (Plafker, 1987). Bruns (1983) inferred the Yakutat microplate itself would have had to have rotated about 45° for the transition fault to have accommodated significant strike-slip motion in the past, but this interpretation did not consider past relative Pacific plate motion changes. Based on plate circuit reconstructions, Doubrovine and Tarduno (2008) determine the azimuth of the Northeastern Pacific plate convergence with south-east Alaska, between ca 40 and 35 Ma, would have been 20° counter-clockwise from the present day Pacific plate vector. Based on limited paleomagnetic data, Van Alstine et al. (1985) inferred the Yakutat microplate may have rotated up to 20° counter-clockwise, hence it is conceivable there was a short period of time when the transition fault was a favorably orientated transform fault boundary dissecting the Yakutat microplate (Fig. 12).

This reconstruction fits published models where the eastern Yakutat microplate was temporarily docked with North America during the slab's northward translation (Bruns, 1983; Plafker et al., 1994; Worthington et al., 2012). During this Eocene docking, it is inferred Cretaceous Chugach-like accretionary-complex rocks were overthrust the ca. 50 Ma Yakutat oceanic plateau (Bruhn et al., 2004; e.g. Worthington et al., 2012). The juxtaposition of Chugach like terrane rocks on top of the eastern Yakutat microplate, Chugach terrane rocks across the Boundary fault in the Boundary Block (Cowan, 1982, 2003), and similarly across the Fairweather fault in the Fairweather Range Block (e.g. Pavlis and Roeske, 2007) (Fig. 1B) is a likely result of terrane dissection, slivering and translation. Additionally, the possibility that the Boundary and Transition faults were paleo-transform boundaries adds further credence to the notion that it is difficult to assign paleobiogeographic, paleomagnetic, and detrital zircon constrained long-distance translation to individual faults deeper in time as faults can be rotated, subducted, and/or fault bound blocks can be dissected (i.e. Baja-B.C. controversy; Cowan, 1982, 2003; Keppie and Dostal, 2001; Wyld et al., 2006; Garver and Davidson, 2015; e.g. Tikoff et al., 2022).

Using Northeast Pacific plate motion rates and North America convergence angle (Doubrovine and Tarduno, 2008) and a simple vector analysis we can approximate the amount of strike-slip along the Fairweather fault since ca. 30 Ma. We obtained a total of 1300 km of permissible horizontal slip along the Fairweather transform boundary since ca. 30 Ma (Table S1O). The traditional seismically imaged maximum length of the unsubducted and subducted Yakutat slab is about 900 km from offshore to the leading edge (Eberhart-Phillips et al., 2006; Mann et al., 2022). However, it is assumed there is likely more Yakutat slab in front of the leading edge that has been eclogized and hence not imageable (Rossi et al., 2006; Rondenay et al., 2008, 2010), and oceanic plateaus are known to be features of great length as lavas run downhill from plume head-ridge source highs (Richards et al., 1991; e.g. Kerr and Mahoney, 2007). A more recent teleseismic, body-wave tomography model (Pavlis et al., 2024) determined the full Yakutat slab was ~1700 km in south to north length. Hence, the full extent of the length of the Yakutat microplate likely is at least 1300 km given the permissible total slip along the Fairweather fault (the Yakutat-North America transform boundary) assuming a ca. 30 Ma initiation.

5.5. Earthquake patterns and block motion

There is limited seismicity between the Fairweather fault and the Border Ranges fault within the Fairweather Range block (Fig. 3). This observation, together with the lack of known active structures internal to the Fairweather Range, and the slight eastward dip of this structure (Ten Brink et al., 2018) suggest that the Fairweather Range is being vertical extruded as a coherent block and ramping up on the Fairweather fault. This interpretation is reinforced by evidence that the Fairweather Range is rheologically stronger than the neighboring Yakutat slab (Ten Brink et al., 2018) which is currently internally deforming (Witter et al., 2023) as evidenced by high seismicity (Fig. 3).

As noted earlier, the Fairweather Range block is composed primarily of accretionary prism rocks of the Chugach terrane that were intruded by near trench plutons during a ridge subduction event during coeval metamorphism. Scharman et al. (2012) examined if the western Chugach metamorphic complex (west of the St. Elias Convergent corner) (Fig. 1) was acting like a coherent block. Based on the presence of limited recorded seismic activity, strength profiles, and the presence of a mafic root they concluded that the Paleocene-Eocene ridge subduction event stabilized the crust of the Chugach terrane. They inferred this crustal stabilization likely facilitates the western Chugach terrane acting as a coherent block with limited internal deformation, similar to the Fairweather Range block.

Seismicity exists along the Border Ranges fault (Figs. 3 and 4) and to the east of this structure. Geodetic results with the Border Ranges fault as an additional block boundary was not considered by Elliott and Freymueller (2020). By replacing their evoked east-west northern boundary (magenta dashed line Fig. 3A) for their evoked Baranof block with the Border Ranges fault as a block boundary leads to a better grouping of geodetic motion data. We infer, based on the difference in block motions between the Fairweather Range block (north-west directed) and the Border Ranges block (north-east directed) as well as the seismicity along and to the east of the Border Ranges fault that this structure is active today likely as a primarily dip-slip fault (Figs. 3 and 13).

5.6. Fairweather fault orogenesis and ca. 3 Ma Yakutat microplate rotation

Based on the entirety of the geochronology and thermochronology data sets presented here as well as the cooling trajectories, we infer the Fairweather Range block has been vertically extruding between the Fairweather and Border Ranges faults since ca. 25 Ma as a generally coherent block (Figs. 3, 4, 9, 10 and 13). Hence these two structures

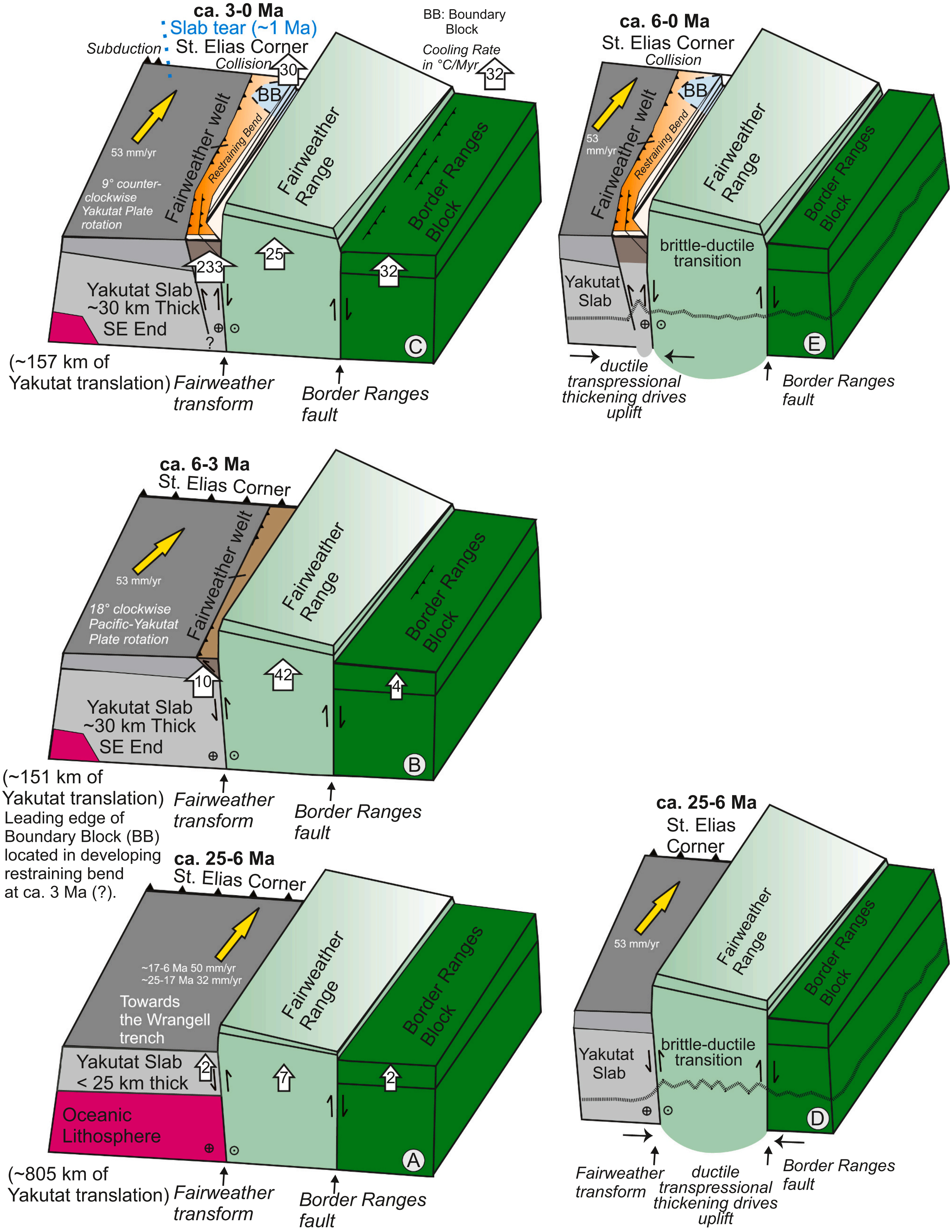

(caption on next page)

Fig. 13. Schematic of the rock cooling history of the Fairweather welt, Fairweather Range block, and Border Ranges block for ca. 25–6 Ma, ca. 6–3 Ma, and ca. 3–0 Ma time periods. The yellow arrow is the general direction of inferred and measured Yakutat slab relative plate motion. Figure not drawn to scale. (A) The Fairweather transform boundary underwent an increase in transpressional deformation by ca. 25 Ma, evidenced by the Fairweather Range block being vertically extruded between the Border Ranges and Fairweather faults. (B) Inferred plate boundary convergence increased across the Fairweather fault, with the ca. 6 Ma Pacific-Yakutat relative plate motion rotation and increase in velocity (Fig. 11). (C) We infer at ca.3 Ma the 20–25 km thick segment of the Yakutat microplate (Worthington et al., 2012) entered the Wrangell trench leading to the counter-clockwise rotation of the Yakutat microplate relative plate motion. The Yakutat slab rotation likely impinged the Fairweather fault and led to the development of the Fairweather restraining bend at this time. With the development of the Fairweather restraining bend the thickened Fairweather welt and ∼ 30 km thick Yakutat oceanic plateau butt-end (Worthington et al., 2012) made for double indenters into the St. Elias convergent margin corner leading to dynamic orogenesis (Enkelmann et al., 2015b; Schartman et al., 2019). We do not depict the rapid ∼80–120 °C/Ma cooling rates for the leading edge of the Boundary Block initiating after ca. 5 Ma, when this block may have been located along the developing Fairweather Fault nascent restraining bend, before being translated northward via strike-slip to its present position and slower cooling (∼30 °C/Ma after ca. 2 Ma) (Figs. 1 and 3) (Schartman et al., 2019). Cooling rates remained high, but decreased in the Fairweather Range block at ca. 3 Ma. Cooling rates increased in the Border Ranges block at this time, particularly away from the fault to the east (Figs. 9 and 10). (D) and (E) Demonstrate crustal thickening through transpressional ductile deformation (e.g. Hollister and Andronicos, 2006). The amount of northward translation of the Yakutat microplate for each time period is shown on the bottom left of each schematic. St. Elias convergent corner shown and ca. 1 Ma slab tear north of the "trench" (Mann et al., 2022; Brueseke et al., 2023b) and west-east transition from subduction to collision shown. (For interpretation of the references to colour in this figure legend, the reader is referred to the web version of this article.)

were active continuously from ca. 25 Ma to the present with a dip-slip component. Vertical block extrusion along paired fault systems is likely common along transpressive transform faults given the history of multiple terrane accretionary events along convergent margins and the prominence of older structures capable of reactivation (Spotila et al., 2001; Selander et al., 2012; Massey and Moecher, 2013; Moser et al., 2017; Klepeis, 2019; Benowitz et al., 2022a; Huang et al., 2023; Moulin and Cowgill, 2023; Roquer et al., 2023). Particularly significant may be crustal thickening at depth resulting from ductile transpressional strain (Sanderson and Marchini, 1984; Fossen et al., 1994), because there is no evidence for faults to accommodate the rock uplift between the Fairweather and Border Ranges faults.

Cooling rates and inferred exhumation rates increased dramatically in the Fairweather Range sometime after 10–14 Ma (Fig. 10). Furthermore, cooling rates increased in the Border Ranges block after ca. 6 Ma (Figs. 7 and 10) (McAleer et al., 2009). We speculatively propose these changes likely occurred in response to the ca. 6 Ma relative Pacific-Yakutat plate motion change (e.g. Austermann et al., 2011). The late Miocene southern Alaska tectonic event has been documented by numerous previous thermochronology (Fitzgerald and Malusà, 2019; Haeussler et al., 2008; Arkle et al., 2013; Waldien et al., 2018; Benowitz et al., 2022a, 2022b) and magmatic (Richter et al., 1990; Jicha et al., 2006; Mukasa et al., 2007; Trop et al., 2022) studies across southern Alaska. This increase in southern Alaska tectonism has been linked to the relative Pacific-Yakutat plate vector change at ca. 6 Ma to more orthogonal (Austermann et al., 2011; Choi et al., 2021; Allen et al., 2022; e.g. Rosenthal et al., 2023). Faults along the circum-Pacific responded to the ca. 6 Ma Pacific plate motion change (Queen Charlotte-Hyndman, 2015; San Andreas-Townsend et al., 2021; La Cruz Fault Baja-Bennett et al., 2016; Alpine Fault-Collett et al., 2019). Since the ca. 6 Ma Pacific plate vector change affected faults across the circum-Pacific we discount southward thickening variation in the Yakutat microplate crust (Worthington et al., 2012) being the main increase in stress along the Fairweather fault at this time, although this thickened crust likely played a role in orogenesis along the Fairweather fault corridor.

Yakutat microplate subduction and collision is a 3-dimensional process (McAleer et al., 2009; Falkowski et al., 2014, 2016). The 30-km-thick portion of the Yakutat microplate that is now colliding would have been ∼310 km outboard of the southern Alaska trench at ca. 6 Ma based on a restored modern Northeastern Pacific-Yakutat plate/North America ∼53 km/Ma convergence rate (e.g. Pavlis et al., 2004; Worthington et al., 2012; Elliott and Freymueller, 2020; Brueseke et al., 2023b). Hence, the Yakutat thick wedge would have been along the southern tip of the Fairweather fault at or slightly before ca.6 Ma and likely played a role in orogenesis along this transform system (McAleer et al., 2009; e.g. Koons et al., 2010; Pavlis et al., 2012). This orogenesis would have led to crustal thickening along the west margin of the Fairweather fault, creating a welt of thicker crust. This Fairweather welt (including the Boundary Block), combined with the thick eastern Yakutat slab would lead to a double indenter scenario into the St. Elias tectonic corner (Figs. 1, 3, and 13).

Coupling at the St. Elias corner southeastern plate interface increased as the thicker part (∼20–30 km; Worthington et al., 2012) of the Yakutat oceanic plateau and the modestly thickened post ca. 6 Ma Fairweather welt entered the Wrangell trench by ca. 3 Ma. Subduction of slabs with varying along strike thickness variations, like the Yakutat slab (Mann et al., 2022), is known to lead to microplate rotation (Wells and Heller, 1988; Wallace et al., 2005; e.g. Wang et al., 2024). We suggest that this nascent "collision" of these Yakutat indenters led to a 9° rotation of the Yakutat microplate and a change in Yakutat slab relative plate motion.

The exhumation history of the Fairweather Range block is consistent with the idea that the Yakutat microplate impinged along the southern Fairweather fault at ca. 3 Ma leading to the formation of the Fairweather restraining bend at this time and vertical extrusion of crustal material between the Icy Point-Lituya Bay and Fairweather faults (Witter et al., 2023) (Figs. 3 and 13). We infer an increase in post ca. 3 Ma transpressional deformation (McAleer et al., 2009, Lease et al., 2021; this study) and topography along the Fairweather welt led to overall increased thickening (Figs. 10 and 13). Exhumation rates increased dramatically along the south-eastern aspect of the St. Elias corner (Falkowski et al., 2014; Enkelmann et al., 2015a, 2015b; Schartman et al., 2019) as the thickened Fairweather welt and the southeast thicker part of the Yakutat oceanic plateau led to stalled subduction, eventually leading to Yakutat slab tearing (Fig. 1) (Mann et al., 2022) and actual collision (Brueseke et al., 2023b). Similar double indenter tectonics have occurred along the Sagaing fault with India and the Burma terrane and associated salients colliding into the eastern Himalayan corner (e.g. Morley et al., 2021; Zhang et al., 2022).

6. Conclusion

The orogenic history of the Fairweather transform boundary region is illuminated by an examination of geochronology and thermochronology of 124 analyses from 81 individual samples and seismicity and geodetic data. The long history of exhumation indicates the Fairweather transform boundary initiated by ca. 30 Ma, consistent with prior ideas on the history of the fault (Plafker et al., 1994). Major results and interpretations of this study on the Fairweather transform boundary region follow:

1) Rapid vertical extrusion of the Fairweather Range block between and on the Fairweather and Border Ranges faults likely began synchronously with the ca. 25 Ma Pacific-Yakutat plate vector change (Jicha et al., 2018). The Border Ranges system has experienced west side up dip-slip movement since ca. 25 Ma.
2) Cooling rates increased in the Fairweather welt, Fairweather Range, and Border Ranges blocks sometime after 10–14 Ma, perhaps nearer to ca. 6 Ma with the Pacific plate vector change at this time

(Austermann et al., 2011). These cooling rates are indicative of ductile transpressional crustal thickening. Post ca. 6 Ma crustal thickening of the Fairweather welt led to an initial double indenter situation in the southeastern St. Elias convergent corner.

3) At ca. 3 Ma we suggest this double indenter situation led to the Yakutat microplate-vector being rotated ~9° counter-clockwise leading to impingement along the Fairweather fault and development of the Fairweather restraining bend. Dramatic, but short-lived (<1 Ma) cooling rates (>200 °C/Ma) and exhumation rates (up to 10 km/Ma) (Lease et al., 2021) along the Fairweather welt are indicative of increased transpressional uplift (Witter et al., 2023) and inferred additional crustal thickening. The indentation of the further thickened Fairweather welt and 20–30 km thick southeast end of the Yakutat oceanic plateau amplified the double indenter scenario in the St. Elias convergent corner (Fig. 13).
4) Overall exhumation rates are slower on the convex side of the Fairweather restraining bend compared to the concave side, but the fixed position of the Fairweather Range block relative to the Fairweather fault has led to persistent and deeper overall exhumation since ca. 25 Ma.
5) Vertical block extrusion along paired fault systems and double-indenter tectonics is likely common along transpressive transform boundaries leading into convergent margin corners.
6) Records of strike-slip motion and paleo-transforms can be obscured by subduction of geologic features (i.e. structures), microplate rotation, and, terrane dissection/slivering and translation.

CRediT authorship contribution statement

Jeff Apple Benowitz: Conceptualization, Data curation, Formal analysis, Methodology, Visualization, Writing – original draft, Writing – review & editing. **Richard Lease**: Conceptualization, Visualization, Writing – review & editing. **Peter J. Haeussler**: Conceptualization, Visualization, Writing – review & editing. **Terry Pavlis**: Visualization, Writing – original draft, Writing – review & editing. **Michael Everett Mann**: Visualization, Writing – review & editing.

Declaration of competing interest

The authors declare that they have no known competing financial interests or personal relationships that could have appeared to influence the work reported in this paper.

Data availability

The data supporting these conclusions can be found in Zenodo Data (DOI https://doi.org/10.5281/zenodo.10909245).

Acknowledgments

The clarity and overall science of the manuscript benefited from discussions and insight from Ken Ridgway, internal USGS manuscript reviews by Robert McDermott and Ric Wilson, and shepherding by editor Samuel Angiboust, and journal reviews by Bruce Idleman and an anonymous reviewer. Any use of trade, firm, or product names is for descriptive purposes only and does not imply endorsement by the U.S. Government.

Appendix A. Supplementary data

Supplementary data to this article can be found online at https://doi.org/10.1016/j.tecto.2024.230337.

References

Agarwal, R.P., 2020. Pythagorean theorem before and after Pythagoras. Adv. Stud. Contemp. Math. 30 (3), 357–389.

Allen, W.K., Ridgway, K.D., Benowitz, J.A., Waldien, T.S., Roeske, S.M., Fitzgerald, P.G., Gillis, R.J., 2022. Neogene sedimentary record of the evolution of a translated strike-slip basin along the Denali fault system: implications for timing of displacement, composite basin development, and regional tectonics of southern Alaska. Geosphere 18 (2), 585–615.

Arkle, J.C., Armstrong, P.A., Haeussler, P.J., Prior, M.G., Hartman, S., Sendziak, K.L., Brush, J.A., 2013. Focused exhumation in the syntaxis of the western Chugach Mountains and Prince William Sound, Alaska. Bulletin 125 (5–6), 776–793.

Austermann, J., Bird, P., Heidbach, O., Schubert, G., Stock, J.M., 2011. Quantifying the forces needed for the rapid change of Pacific plate motion at 6 Ma. Earth Planet. Sci. Lett. 307 (3–4), 289–297.

Barth, N.C., Boulton, C., Carpenter, B.M., Batt, G.E., Toy, V.G., 2013. Slip localization on the southern Alpine fault, New Zealand. Tectonics 32 (3), 620–640.

Batt, G.E., Baldwin, S.L., Cottam, M.A., Fitzgerald, P.G., Brandon, M.T., Spell, T.L., 2004. Cenozoic plate boundary evolution in the South Island of New Zealand: new thermochronological constraints. Tectonics 23 (4).

Bennett, S.E., Oskin, M.E., Iriondo, A., Kunk, M.J., 2016. Slip history of the La Cruz fault: development of a late Miocene transform in response to increased rift obliquity in the northern Gulf of California. Tectonophysics 693, 409–435.

Benowitz, J.A., Layer, P.W., Armstrong, P., Perry, S.E., Haeussler, P.J., Fitzgerald, P.G., VanLaningham, S., 2011. Spatial variations in focused exhumation along a continental-scale strike-slip fault: the Denali fault of the eastern Alaska Range. Geosphere 7 (2), 455–467.

Benowitz, J.A., Layer, P.W., VanLaningham, S., 2014. Persistent Long-Term (c. 24 Ma) Exhumation in the Eastern Alaska Range Constrained by Stacked Thermochronology. The Geological Society of London, London.

Benowitz, J.A., Davis, K., Roeske, S., 2019. A river runs through it both ways across time: ^{40}Ar/^{39}Ar detrital and bedrock muscovite geochronology constraints on the Neogene paleodrainage history of the Nenana River system, Alaska Range. Geosphere 15 (3), 682–701.

Benowitz, J.A., Roeske, S.M., Regan, S.P., Waldien, T.S., Elliott, J.L., O'Sullivan, P.B., 2022a. Large-scale, crustal-block vertical extrusion between the Hines Creek and Denali faults coeval with slip localization on the Denali fault since ca. 45 Ma, Hayes Range, Alaska, USA. Geosphere 18 (3), 1030–1054.

Benowitz, J.A., Cooke, M.L., Terhune, P.J., Herreid, S., Bemis, S.P., Toeneboehn, K., Waldien, T.S., O'Sullivan, P.B., 2022b. Why is Denali (6,194 m) so big? Caught inside the tectonic wake of a migrating restraining bend. Terra Nova 34 (2).

Berkelhammer, S.E., Brueseke, M.E., Benowitz, J.A., Trop, J.M., Davis, K., Layer, P.W., Weber, M., 2019. Geochemical and geochronological records of tectonic changes along a flat-slab arc-transform junction: Circa 30 Ma to ca. 19 Ma Sonya Creek volcanic field, Wrangell Arc, Alaska. Geosphere 15 (5), 1508–1538.

Bernet, M., 2009. A field-based estimate of the zircon fission-track closure temperature. Chem. Geol. 259 (3–4), 181–189.

Brandon, M.T., 1992. Decomposition of fission-track grain-age distributions. Am. J. Sci. 292 (8), 535–564.

Brandon, M.T., 1996. Probability density plot for fission-track grain-age samples. Radiat. Meas. 26 (5), 663–676.

Brew, D.A., Tellier, K.E., Lanphere, M.A., Nielsen, D.C., Smith, J.G., Sonnevil, R.A., 2014. Geochronology of Plutonic Rocks and their Tectonic Terranes in Glacier Bay National Park and Preserve, Southeast Alaska: Chapter E in Studies by the US Geological Survey in Alaska, 2008-2009 (No. 1776-E). US Geological Survey.

Brothers, D.S., Miller, N.C., Barrie, J.V., Haeussler, P.J., Greene, H.G., Andrews, B.D., Zielke, O., Watt, J., Dartnell, P., 2020. Plate boundary localization, slip-rates and rupture segmentation of the Queen Charlotte Fault based on submarine tectonic geomorphology. Earth Planet. Sci. Lett. 530 (115882) https://doi.org/10.1016/j.epsl.2019.115882.

Brueseke, M.E., Benowitz, J.A., Trop, J.M., Davis, K.N., Berkelhammer, S.E., Layer, P.W., Morter, B.K., 2019. The Alaska Wrangell Arc: ~ 30 Ma of subduction-related magmatism along a still active arc-transform junction. Terra Nova 31 (1), 59–66.

Brueseke, M., Morter, B.K., Benowitz, J.A., Trop, J., Mertzman, S.A., Kirby, C.S., Davis, K., 2023a. What lies beneath the ice? Using the geochemistry and geochronology of modern river cobbles to better decipher the evolution of a glaciated volcanic arc (Wrangell Arc, Alaska, USA). Volcanica 6 (2), 313–329.

Brueseke, M.E., Benowitz, J.A., Bearden, A.T., Mann, M.E., Miggins, D.P., 2023b. Subduction disruption, slab tears: Ca. 1 Ma true collision of an ~30-km-thick oceanic plateau segment recorded by Yakutat slab nascent tear magmatism. Terra Nova 35, 49–57. https://doi.org/10.1111/ter.12628.

Bruhn, R.L., Pavlis, T.L., Plafker, G., Serpa, L., 2004. Deformation during terrane accretion in the Saint Elias orogen, Alaska. Geological Society of America Bulletin 116 (7–8), 771–787.

Bruns, T.R., 1983. Model for the origin of the Yakutat block, an accreting terrane in the northern Gulf of Alaska. Geology 11 (12), 718–721.

Chapman, J.B., Pavlis, T.L., Bruhn, R.L., Worthington, L.L., Gulick, S.P., Berger, A.L., 2012. Structural relationships in the eastern syntaxis of the St. Elias orogen, Alaska. Geosphere 8 (1), 105–126.

Choi, M., Eaton, D.W., Enkelmann, E., 2021. Is the Eastern Denali fault still active? Geology 49 (6), 662–666.

Christeson, G.L., Gulick, S.P., van Avendonk, H.J., Worthington, L.L., Reece, R.S., Pavlis, T.L., 2010. The Yakutat terrane: dramatic change in crustal thickness across the transition fault, Alaska. Geology 38 (10), 895–898.

Collett, C.M., Duvall, A.R., Flowers, R.M., Tucker, G.E., Upton, P., 2019. The timing and style of oblique deformation within New Zealand's Kaikōura ranges and

Marlborough fault system based on low-temperature thermochronology. Tectonics 38 (4), 1250–1272.

Cowan, D.S., 1982. Geological evidence for post–40 my BP large-scale northwestward displacement of part of southeastern Alaska. Geology 10 (6), 309–313.

Cowan, D.S., 2003. Revisiting the Baranof–Leech River hypothesis for early Tertiary coastwise transport of the Chugach–Prince William terrane. Earth Planet. Sci. Lett. 213 (3–4), 463–475.

Crowell, J.C., 1974. Origin of late Cenozoic basins in southern California. In: Tectonics and Sedimentation, vol. 22. Society of Economic Paleontologists and Mineralogists, Tulsa, Okla, pp. 190–204.

Davids, C., Benowitz, J.A., Layer, P.W., Bergh, S.G., 2018. Direct ^{40}Ar/^{39}Ar K-feldspar dating of late Permian—early Triassic brittle faulting in northern Norway. Terra Nova 30 (4), 263–269.

Dorsey, R.J., Langenheim, V.E., 2015. Crustal-scale tilting of the central Salton block, southern California. Geosphere 11 (5), 1365–1383.

Doubrovine, P.V., Tarduno, J.A., 2008. A revised kinematic model for the relative motion between Pacific oceanic plates and North America since the late cretaceous. J. Geophys. Res. Solid Earth 113, 1–20.

Eberhart-Phillips, D., Christensen, D.H., Brocher, T.M., Hansen, R., Ruppert, N.A., Haeussler, P.J., Abers, G.A., 2006. Imaging the transition from Aleutian subduction to Yakutat collision in Central Alaska, with local earthquakes and active source data. J. Geophys. Res. Solid Earth 111 (B11).

Elliott, J., Freymueller, J.T., 2020. A block model of present-day kinematics of Alaska and Western Canada. J. Geophys. Res. Solid Earth 125. https://doi.org/10.1029/2019JB018378.

Engebretson, D.C., Cox, A., Gordon, R.G., 1985. Relative motions between oceanic and continental plates in the Pacific Basin. Geol. Soc. Am. Spec. Pap. 206, 59. https://doi.org/10.1130/SPE206-p1.

Enkelmann, E., Garver, J.I., Pavlis, T.L., 2008. Rapid exhumation of ice-covered rocks of the Chugach–St. Elias orogen, Southeast Alaska. Geology 36 (12), 915–918.

Enkelmann, E., Valla, P.G., Champagnac, J.D., 2015a. Low-temperature thermochronology of the Yakutat plate corner, St. Elias Range (Alaska): bridging short-term and long-term deformation. Quat. Sci. Rev. 113, 23–38.

Enkelmann, E., Koons, P.O., Pavlis, T.L., Hallet, B., Barker, A., Elliott, J., Garver, J.I., Gulick, S.P., Headley, R.M., Pavlis, G.L., Ridgway, K.D., 2015b. Cooperation among tectonic and surface processes in the St. Elias Range, Earth's highest coastal mountains. Geophys. Res. Lett. 42 (14), 5838–5846.

Falkowski, S., Enkelmann, E., 2016. Upper-crustal cooling of the Wrangellia composite terrane in the northern St. Elias Mountains, western Canada. Lithosphere 8 (4), 359–378.

Falkowski, S., Enkelmann, E., Ehlers, T.A., 2014. Constraining the area of rapid and deep-seated exhumation at the St. Elias syntaxis, Southeast Alaska, with detrital zircon fission-track analysis. Tectonics 33 (5), 597–616.

Falkowski, S., Enkelmann, E., Drost, K., Pfaender, J.A., Stuebner, K., Ehlers, T.A., 2016. Cooling history of the St. Elias syntaxis, Southeast Alaska, revealed by geochronology and thermochronology of cobble-sized glacial detritus. Tectonics 35 (2), 447–468.

Farley, K.A., 2000. Helium diffusion from apatite: general behavior as illustrated by Durango fluorapatite. J. Geophys. Res. Solid Earth 105 (B2), 2903–2914.

Fattaruso, L.A., Cooke, M.L., Dorsey, R.J., 2014. Sensitivity of uplift patterns to dip of the San Andreas fault in the Coachella Valley, California. Geosphere 10 (6), 1235–1246.

Feldberg-Bannatyne, M., Davidson, C., Garver, J.I., 2023. U-Pb zircon geochronology and LU-HF isotope study of the Sanak-Baranoff belt in Southeast Alaska: a focus on the intrusive bodies of the Yakobi Island, Chichagof Island, and Glacier Bay National Park. Geol. Soc. Am. Abstr. Programs 55 (4). https://doi.org/10.1130/abs/2023CD-387416.

Ferris, A., Abers, G.A., Christensen, D.H., Veenstra, E., 2003. High resolution image of the subducted Pacific (?) plate beneath Central Alaska, 50-150 km depth. Earth Planet. Sci. Lett. 214 (3–4), 575–588.

Finlayson, V.A., Konter, J.G., Konrad, K., Koppers, A.A.P., Jackson, M.G., Rooney, T.O., 2018. Sr–Pb–Nd–Hf isotopes and 40Ar/39Ar ages reveal a Hawaii–Emperor-style bend in the Rurutu hotspot. Earth Planet. Sci. Lett. 500, 168–179.

Fitzgerald, P.G., Malusà, M.G., 2019. Concept of the exhumed partial annealing (retention) zone and age-elevation profiles in thermochronology. In: Fission-Track Thermochronology and its Application to Geology, pp. 165–189.

Fossen, H., Tikoff, B., Teyssier, C., 1994. Strain modeling of transpressional and transtensional deformation. Nor. Geol. Tidsskr. 74 (3), 134–145.

Fuis, G.S., Scheirer, D.S., Langenheim, V.E., Kohler, M.D., 2012. A new perspective on the geometry of the San Andreas fault in southern California and its relationship to lithospheric structure. Bull. Seismol. Soc. Am. 102 (1), 236–251.

Gaastra, K.M., Gordon, R.G., Woodworth, D.T., 2022. Quantification of Pacific plate hotspot tracks since 80 Ma. Tectonics 41 (7) e2021TC006772.

Gaber, L.J., Foland, K.A., Corbato, C.E., 1988. On the significance of Ar release from biotite and amphibole during 40Ar/39Ar vacuum heating. Geochim. Cosmochim. Acta 52, 2457–2465.

Garver, J.I., Davidson, C.M., 2015. Southwestern Laurentian zircons in Upper Cretaceousflysch of the Chugach-Prince William terrane in Alaska. Am. J. Sci. 315, 537–556. https://doi.org/10.2475/06.2015.02.

Gasser, D., Bruand, E., Stüwe, K., Foster, D.A., Schuster, R., Fügenschuh, B., Pavlis, T., 2011. Formation of a metamorphic complex along an obliquely convergent margin: structural and thermochronological evolution of the Chugach Metamorphic complex, southern Alaska. Tectonics 30 (2).

Gasser, D., Rubatto, D., Bruand, E., Stüwe, K., 2012. Large-scale, short-lived metamorphism, deformation, and magmatism in the Chugach metamorphic complex, southern Alaska: a SHRIMP U-Pb study of zircons. Bulletin 124 (5–6), 886–905.

Grove, M., Harrison, T.M., 1996. ^{40}Ar* diffusion in Fe-rich biotite. Am. Mineral. 81 (7–8), 940–951.

Gulick, S.P., Lowe, L.A., Pavlis, T.L., Gardner, J.V., Mayer, L.A., 2007. Geophysical insights into the transition fault debate: propagating strike slip in response to stalling Yakutat block subduction in the Gulf of Alaska. Geology 35 (8), 763–766.

Haeussler, P.J., O'Sullivan, P., Berger, A.L., Spotila, J.A., 2008. Neogene exhumation of the Tordrillo Mountains, Alaska, and correlations with Denali (Mount McKinley). In: Washington DC American Geophysical Union Geophysical Monograph Series, 179, pp. 269–285.

Harding, T.P., 1985. Seismic characteristics and identification of negative flower structures, positive flower structures, and positive structural inversion. AAPG Bull. 69 (4), 582–600.

Harrison, T.M., 1982. Diffusion of ^{40}Ar in hornblende. Contrib. Mineral. Petrol. 78, 324–331.

Harrison, T.M., Célérier, J., Aikman, A.B., Hermann, J., Heizler, M.T., 2009. Diffusion of ^{40}Ar in muscovite. Geochim. Cosmochim. Acta 73 (4), 1039–1051.

Herman, F., Cox, S.C., Kamp, P.J., 2009. Low-temperature thermochronology and thermokinematic modeling of deformation, exhumation, and development of topography in the central Southern Alps, New Zealand. Tectonics 28 (5).

Hollister, L.S., Andronicos, C.L., 2006. Formation of new continental crust in Western British Columbia during transpression and transtension. Earth Planet. Sci. Lett. 249 (1–2), 29–38.

Holm-Denoma, C.S., Pianowski, L.S., Wilson, F.H., 2020. U-Pb Zircon Data for: Cretaceous Plutonic Rocks of Western Glacier Bay National Park and Preserve: U.S. Geological Survey Data Release. https://doi.org/10.5066/P90HNEP5.

Huang, J., Lin, X., An, K., Chen, H., Cheng, X., Qu, Y., Li, Y., Yang, X., Zhang, L., Chen, C., Chen, Z., 2023. Long-lived Cenozoic positive relief of the south-Eastern Tian Shan: insights from provenance analyses of the northwestern Kuqa depression sediments. Palaeogeogr. Palaeoclimatol. Palaeoecol. 111846.

Hudson, T., Plafker, G., Turner, D.L., 1977a. Metamorphic rocks of the Yakutat–St. Elias area, south-Central Alaska. J. Res. US Geol. Surv. 5 (2), 173–184.

Hudson, T., Plafker, G., Lanphere, M.A., 1977b. Intrusive rocks of the Yakutat-St. Elias area, south-Central Alaska. J. Res. US Geol. Surv. 5, 155–172.

Hyndman, R., 2015. Tectonics and structure of the Queen Charlotte fault zone, Haida Gwaii, and large thrust earthquakes. Bull. Seismol. Soc. Am. 105 (2B), 1058–1075.

Jicha, B.R., Scholl, D.W., Singer, B.S., Yogodzinski, G.M., Kay, S.M., 2006. Revised age of Aleutian Island Arc formation implies high rate of magma production. Geology 34 (8), 661–664.

Jicha, B.R., Garcia, M.O., Wessel, P., 2018. Mid-Cenozoic Pacific plate motion change: implications for the northwest Hawaiian Ridge and circum-Pacific. Geology 46 (11), 939–942.

Kamp, P.J., 1991. Late. Oligocene Pacific-wide tectonic event. Terra Nova 3 (1), 65–69.

Keppie, J.D., Dostal, J., 2001. Evaluation of the Baja controversy using paleomagnetic and faunal data, plume magmatism, and piercing points. Tectonophysics 339 (3–4), 427–442.

Kerr, A.C., Mahoney, J.J., 2007. Oceanic plateaus: problematic plumes, potential paradigms. Chem. Geol. 241 (3–4), 332–353.

Ketcham, R.A., Donelick, R.A., Carlson, W.D., 1999. Variability of apatite fission-track annealing kinetics: III. Extrapolation to geological time scales. Am. Mineral. 84 (9), 1235–1255.

Klepeis, K., 2019. Deep slab collision during Miocene subduction causes uplift along crustal-scale reverse faults in Fiordland, New Zealand, *GSA today*.

Koons, P.O., Hooks, B.P., Pavlis, T., Upton, P., Barker, A.D., 2010. Three-dimensional mechanics of Yakutat convergence in the southern Alaskan plate corner. Tectonics 29 (4).

Lease, R.O., Haeussler, P.J., Witter, R.C., Stockli, D.F., Bender, A.M., Kelsey, H.M., O'Sullivan, P.B., 2021. Extreme Quaternary plate boundary exhumation and strike-slip localized along the southern Fairweather fault, Alaska, USA. Geology 49 (5), 602–606.

Little, T.A., Cox, S., Vry, J.K., Batt, G., 2005. Variations in exhumation level and uplift rate along the oblique-slip Alpine fault, central Southern Alps, New Zealand. Geol. Soc. Am. Bull. 117 (5–6), 707–723.

Löbens, S., Oriolo, S., Benowitz, J., Wemmer, K., Layer, P., Siegesmund, S., 2017. Late Paleozoic deformation and exhumation in the Sierras Pampeanas (Argentina): ^{40}Ar/^{39} Ar-feldspar dating constraints. International Journal of Earth Sciences 106, 1991–2003.

Lovera, O.M., Grove, M., Harrison, T.M., Mahon, K.I., 1997. Systematic analysis of K-feldspar 40Ar39Ar step heating results: I. Significance of activation energy determinations. Geochim. Cosmochim. Acta 61 (15), 3171–3192.

Ludwig, K.R., 2012. Isoplot/Ex Version 4.15, A Geochronological Toolkit for Microsoft Excel, vol. 4. Berkeley Geochronology Center Special Publication, Berkeley, California.

Mann, M.E., Abers, G.A., Daly, K., Christensen, D.H., 2022. Subduction of an oceanic plateau across Southcentral Alaska: scattered-wave imaging. J. Geophys. Res. Solid Earth 127 e2021JB022697.

Massey, M.A., Moecher, D.P., 2013. Transpression, extrusion, partitioning, and lateral escape in the middle crust: significance of structures, fabrics, and kinematics in the Bronson Hill zone, southern New England, USA. J. Struct. Geol. 55, 62–78.

McAleer, R.J., Spotila, J.A., Enkelmann, E., Berger, A.L., 2009. Exhumation along the Fairweather fault, southeastern Alaska, based on low-temperature thermochronometry. Tectonics 28 (1).

Morley, C.K., Chantraprasert, S., Kongchum, J., Chenoll, K., 2021. The West Burma Terrane, a review of recent paleo-latitude data, its geological implications and constraints. Earth Sci. Rev. 220, 103722.

Moser, A.C., Evans, J.P., Ault, A.K., Janecke, S.U., Bradbury, K.K., 2017. (U–Th)/He thermochronometry reveals Pleistocene punctuated deformation and synkinematic hematite mineralization in the Mecca Hills, southernmost San Andreas Fault zone. Earth Planet. Sci. Lett. 476, 87–99.

Moulin, A., Cowgill, E., 2023. The Mojave section of the San Andreas Fault (California), 2: Pleistocene records of near-field transpression illuminate the atypical evolution of the restraining “big bend”. Geochem. Geophys. Geosyst. 24 (10) e2023GC010897.

Mukasa, S.B., Andronikov, A.V., Hall, C.M., 2007. The ^{40}Ar/^{39}Ar chronology and eruption rates of Cenozoic volcanism in the eastern Bering Sea Volcanic Province, Alaska. J. Geophys. Res. Solid Earth 112 (B6).

Nabelek, P.I., Hofmeister, A.M., Whittington, A.G., 2012. The influence of temperature-dependent thermal diffusivity on the conductive cooling rates of plutons and temperature-time paths in contact aureoles. Earth Planet. Sci. Lett. 317, 157–164.

Niemi, N.A., Buscher, J.T., Spotila, J.A., House, M.A., Kelley, S.A., 2013. Insights from low-temperature thermochronometry into transpressional deformation and crustal exhumation along the San Andreas fault in the western Transverse Ranges, California. Tectonics 32 (6), 1602–1622.

Norris, R.J., Toy, V.G., 2014. Continental transforms: a view from the Alpine Fault. J. Struct. Geol. 64, 3–31.

O’Sullivan, P.B., Plafker, G., Murphy, J.M., Dumoulin, J.A., Gray, J.E., 1997. Apatite fission-track thermotectonic history of crystalline rocks in the northern Saint Elias Mountains, Alaska. In: Geological Studies in Alaska by the US Geological Survey: US Geological Survey Professional Paper, 1574, pp. 283–294.

Pavlis, T.L., Roeske, S.M., 2007. The border ranges fault system, southern Alaska. In: Ridgeway, K.D., Trop, J.M., Glen, J.M.G., O’Neill, J.M. (Eds.), Tectonic Growth of a Collisional Continental Margin: Crustal Evolution of Southern Alaska: Geological Society of America Special Paper, 431, pp. 95–127.

Pavlis, T.L., Sisson, V.B., 1995. Structural history of the Chugach metamorphic complex in the Tana River region, eastern Alaska: a record of Eocene ridge subduction. Geol. Soc. Am. Bull. 107 (11), 1333–1355.

Pavlis, T.L., Picornell, C., Serpa, L., Bruhn, R.L., Plafker, G., 2004. Tectonic processes during oblique-collision: insights from the St. Elias Orogen, northern north American Cordillera. Tectonics 23, TC3001. https://doi.org/10.1029/2003TC001557, 14p.

Pavlis, G.L., Bauer, M.A., Elliott, J.L., Koons, P., Pavlis, T.L., Ruppert, N., Ward, K.M., Worthington, L.L., 2019. A unified three-dimensional model of the lithospheric structure at the subduction corner in Southeast Alaska: summary results from STEEP. Geosphere 15 (2), 382–406.

Pavlis, T.L., Chapman, J.B., Bruhn, R.L., Ridgway, K., Worthington, L.L., Gulick, S.P., Spotila, J., 2012. Structure of the actively deforming fold-thrust belt of the St. Elias orogen with implications for glacial exhumation and three-dimensional tectonic processes. Geosphere 8 (5), 991–1019.

Pavlis, G., Jadamec, M., Mann, M.E., Yang, X., Schaeffer, A., Wei, S., Fischer, K., 2024. Synthesis of the Seismic Structure of the Greater Alaska Region: Subducting Slab Geometry. AGU Monograph. In Press.

Plafker, G., 1987. Regional geology and petroleum potential of the northern Gulf of Alaska continental margin. In: Scholl, D.W., Grantz, A., Vedder, J.G. (Eds.), Geology and Resource Potential of the Continental Margin of Western North America and Adjacent Ocean Basins, AAPG Circum- Pac. Earth Sci. Ser. 6. American Association of Petroleum Geologists, Houston, Texas, pp. 229–268.

Plafker, G., Hudson, T., Bruns, T., Rubin, M., 1978. Late Quaternary offsets along the Fairweather fault and crustal plate interactions in southern Alaska. Can. J. Earth Sci. 15 (5), 805–816.

Plafker, G., Moore, J.C., Winkler, G.R., 1994. Geology of the southern Alaska margin. In: Plafker, G., Berg, H.C. (Eds.), The Geology of North America: The Geology of Alaska. Geol. Soc. Am, Boulder, Colo, pp. 389–449.

Reiners, P.W., Brandon, M.T., 2006. Using thermochronology to understand orogenic erosion. Annu. Rev. Earth Planet. Sci. 34, 419–466.

Reiners, P.W., Spell, T.L., Nicolescu, S., Zanetti, K.A., 2004. Zircon (U-Th)/He thermochronometry: He diffusion and comparisons with 40Ar/39Ar dating. Geochim. Cosmochim. Acta 68 (8), 1857–1887.

Reiners, P.W., Ehlers, T.A., Zeitler, P.K., 2005. Past, present, and future of thermochronology. Rev. Mineral. Geochem. 58 (1), 1–18.

Renne, P.R., Mundil, R., Balco, G., Min, K., Ludwig, K.R., 2010. Joint determination of 40K decay constants and ^{40}Ar*/^{40}K for the Fish Canyon sanidine standard, and improved accuracy for 40Ar/39Ar geochronology. Geochimica et Cosmochimica Acta 74 (18), 5349–5367.

Richards, M.A., Jones, D.L., Duncan, R.A., DePaolo, D.J., 1991. A mantle plume initiation model for the Wrangellia flood basalt and other oceanic plateaus. Science 254 (5029), 263–267.

Richter, D.H., Smith, J.G., Lanphere, M.A., Dalrymple, G.B., Reed, B.L., Shew, N., 1990. Age and progression of volcanism, Wrangell volcanic field, Alaska. Bull. Volcanol. 53, 29–44.

Roeske, S.M., Pavlis, T.L., Snee, L.W., Sisson, V.B., 1992. 40Ar/39Ar isotopic ages from the combined Wrangellia-Alexander terrane along the border ranges fault system in the eastern Chugach Mountains and Glacier Bay, Alaska. In: Geologic Studies in Alaska by the U.S. Geological Survey, 1990, 1999. U.S. Geological Survey Bulletin, pp. 180–195.

Roeske, S.M., Snee, L.W., Pavlis, T.L., 2003. Dextral-slip reactivation of an arc-forearc boundary during late Cretaceous-early Eocene oblique convergence in the northern Cordillera. In: Sisson, V.B., Roeske, S.M., Pavlis, T.L. (Eds.), Geology of a Transpressional Orogen Developed during Ridge- Trench Interaction along the North Pacific Margin: Geological Society America Special Paper, 371, pp. 141–169.

Rohr, K.M., Currie, L., 1997. Queen Charlotte basin and coast mountains: paired belts of subsidence and uplift caused by a low-angle normal fault. Geology 25 (9), 819–822.

Rondenay, S., Abers, G.A., Van Keken, P.E., 2008. Seismic imaging of subduction zone metamorphism. Geology 36 (4), 275–278.

Rondenay, S., Montési, L.G., Abers, G.A., 2010. New geophysical insight into the origin of the Denali volcanic gap. Geophys. J. Int. 182 (2), 613–630.

Roquer, T., Arancibia, G., Seymour, N.M., Veloso, E.E., Rowland, J., Stockli, D.F., Jöns, N., Morata, D., 2023. Fault-driven differential exhumation in a transpressional tectonic setting: a combined microstructural and thermochronologic approach from the Liquiñe-Ofqui fault system, Southern Andes (39° S). Tectonics 42 (2) e2022TC007229.

Rosenthal, J.R., Fitzgerald, P.G., Benowitz, J.A., Metcalf, J.R., Betka, P.B., 2023. Slip Redistribution onto the Totschunda Fault of Southern Alaska-A Result of a Pacific Plate Motion Change at ca. 6 Ma. AGU Monograph. In Press.

Rossi, G., Abers, G.A., Rondenay, S., Christensen, D.H., 2006. Unusual mantle Poisson’s ratio, subduction, and crustal structure in Central Alaska. J. Geophys. Res. Solid Earth 111 (B9).

Sanderson, D.J., Marchini, W.R.D., 1984. Transpression. J. Struct. Geol. 6 (5), 449–458.

Schaen, A.J., Jicha, B.R., Hodges, K.V., Vermeesch, P., Stelten, M.E., Mercer, C.M., Phillips, D., Rivera, T.A., Jourdan, F., Matchan, E.L., Hemming, S.R., 2021. Interpreting and reporting 40Ar/39Ar geochronologic data. Bulletin 133 (3–4), 461–487.

Scharman, M.R., Pavlis, T.L., Ruppert, N., 2012. Crustal stabilization through the processes of ridge subduction: examples from the Chugach metamorphic complex, southern Alaska. Earth Planet. Sci. Lett. 329, 122–132.

Schartman, A., Enkelmann, E., Garver, J.I., Davidson, C.M., 2019. Uplift and exhumation of the Russell Fiord and boundary blocks along the northern Fairweather transform fault, Alaska. Lithosphere 11 (2), 232–251.

Selander, J., Oskin, M., Ormukov, C., Abdrakhmatov, K., 2012. Inherited strike-slip faults as an origin for basement-cored uplifts: example of the Kungey and Zailiskey ranges, northern Tian Shan. Tectonics 31 (4). https://doi.org/10.1029/2011tc003002.

Sharman, G.R., Graham, S.A., Grove, M., Hourigan, J.K., 2013. A reappraisal of the early slip history of the San Andreas fault, Central California, USA. Geology 41 (7), 727–730.

Sisson, V.B., Pavlis, T.L., 1993. Geologic consequences of plate reorganization: an example from the Eocene southern Alaska fore arc. Geology 21 (10), 913–916.

Sisson, V.B., Poole, A.R., Harris, N.R., Burner, H.C., Pavlis, T.L., Copeland, P., Donelick, R.A., McClelland, W., 2003. Magmatic and geochronologic constraints for genesis of a tonalite-trondhjemite suite and associated mafic intrusive rocks in the eastern Chugach Mountains, Alaska: a record of ridge transform subduction. In: Sisson, V.B., Roeske, S.M., Pavlis, T.L. (Eds.), Geology of a Transpressional Orogen Developed during Ridge-Trench Interaction along the North Pacific Margin: Geological Society of America Special Paper, 371, pp. 293–326.

Smart, K.J., Pavlis, T.L., Sisson, V.B., Roeske, S.M., Snee, L.W., 1996. The border ranges fault system in Glacier Bay National Park, Alaska: evidence for major early Cenozoic dextral strike-slip motion. Can. J. Earth Sci. 33 (9), 1268–1282.

Spotila, J.A., Farley, K.A., Yule, J.D., Reiners, P.W., 2001. Near-field transpressive deformation along the San Andreas fault zone in southern California, based on exhumation constrained by (U-Th)/He dating. J. Geophys. Res. 106 (B12), 30909–30922. https://doi.org/10.1029/2001jb000348.

Spotila, J.A., Niemi, N., Brady, R., House, M., Buscher, J., Oskin, M., 2007a. Long-term continental deformation associated with transpressive plate motion: the San Andreas fault. Geology 35 (11), 967–970.

Spotila, J.A., House, M.A., Niemi, N.A., Brady, R.C., Oskin, M., Buscher, J.T., 2007b. Patterns of Bedrock Uplift along the San Andreas Fault and Implications for Mechanisms of Transpression.

Sylvester, A.G., 1988. Strike-slip faults. Geol. Soc. Am. Bull. 100 (10), 0016–7606.

Ten Brink, U.S., Miller, N.C., Andrews, B.D., Brothers, D.S., Haeussler, P.J., 2018. Deformation of the Pacific/North America plate boundary at Queen Charlotte Fault: the possible role of rheology. J. Geophys. Res. Solid Earth 123 (5), 4223–4242.

Tikoff, B., Housen, B.A., Maxson, J.A., Nelson, E.M., Trevino, S., Shipley, T.F., 2022. Hit-and-run model for Cretaceous–Paleogene tectonism along the western margin of Laurentia. In: Laurentia: Turning Points in the Evolution of a Continent. Geological Society of America.

Tocher, D., 1960. The Alaska earthquake of July 10, 1958: movement on the Fairweather fault and field investigation of southern epicentral region. Bull. Seismol. Soc. Am. 50, 267–292.

Torsvik, T.H., Doubrovine, P.V., Steinberger, B., Gaina, C., Spakman, W., Domeier, M., 2017. Pacific plate motion change caused the Hawaiian-Emperor bend. Nat. Commun. 8 (1), 15660.

Townsend, K.F., Clark, M.K., Niemi, N.A., 2021. Reverse faulting within a continental plate boundary transform system. Tectonics 40 (11) e2021TC006916.

Trop, J.M., Benowitz, J., Cole, R.B., O’Sullivan, P., 2019. Cretaceous to Miocene magmatism, sedimentation, and exhumation within the Alaska Range suture zone: a polyphase reactivated terrane boundary. Geosphere 15 (4).

Trop, J.M., Benowitz, J.A., Kirby, C.S., Brueseke, M.E., 2022. Geochronology of the Wrangell Arc: spatial-temporal evolution of slab-edge magmatism along a flat-slab, subduction-transform transition, Alaska-Yukon. Geosphere 18 (1), 19–48.

Valli, F., Arnaud, N., Leloup, P.H., Sobel, E.R., Mahéo, G., Lacassin, R., Guillot, S., Li, H., Tapponnier, P., Xu, Z., 2007. Twenty million years of continuous deformation along the Karakorum fault, western Tibet: a thermochronological analysis. Tectonics 26 (4).

Van Alstine, D.R., Bazard, D.R., Whitney, J.W., 1985. Paleomagnetism of cores from the Yakutat well. In: Gulf of Alaska (abs.): American Geophysical Union Transactions, 66 (46), 865.a.

Wackett, A.A., Smith, D.R., Davidson, C., Garver, J.I., 2024. New geochemical and geochronological insights on forearc magmatism across the Sanak-Baranof belt, southern Alaska: a tale of two belts. Geosphere. https://doi.org/10.1130/GES02642.1.

Waldien, T.S., Roeske, S.M., Benowitz, J.A., Allen, W.K., Ridgway, K.D., O’Sullivan, P.B., 2018. Late Miocene to Quaternary evolution of the McCallum Creek thrust system, Alaska: insights for range-boundary thrusts in transpressional orogens. Geosphere 14 (6), 2379–2406.

Wallace, L.M., McCaffrey, R., Beavan, J., Ellis, S., 2005. Rapid microplate rotations and backarc rifting at the transition between collision and subduction. Geology 33 (11), 857–860.

Wang, C., Ding, W., Schellart, W.P., Tong, Z., Dong, C., Fang, Y., Li, J., 2024. Effects of along-trench asymmetric subduction initiation on plate rotation and trench migration: a laboratory modeling perspective. Tectonics 43 (1) e2023TC007941.

Wells, R.E., Heller, P.L., 1988. The relative contribution of accretion, shear, and extension to Cenozoic tectonic rotation in the Pacific 4st. Geol. Soc. Am. Bull. 100 (3), 325–338.

Wells, R., Bukry, D., Friedman, R., Pyle, D., Duncan, R., Haeussler, P., Wooden, J., 2014. Geologic history of Siletzia, a large igneous province in the Oregon and Washington coast range: correlation to the geomagnetic polarity time scale and implications for a long-lived Yellowstone hotspot. Geosphere 10 (4), 692–719.

White, T., Bradley, D., Haeussler, P., Rowley, D.B., 2017. Late Paleocene–early Eocene paleosols and a new measure of the transport distance of Alaska's Yakutat Terrane. J. Geol. 125 (2), 113–123.

Wilson, F.H., Hults, C.P., Mull, C.G., Karl, S.M., 2015. Geologic Map of Alaska: U.S. Geological Survey Scientific Investigations Map 3340, Scale 1:1,584,000, 2 Sheets.

Wilson, F.H., Karl, S.M., Shew, N.B., 2021. Geochemical and ^{40}Ar/^{39}Ar Analytical Data of Rocks from Glacier Bay National Park and Preserve: U.S. Geological Survey Data Release. https://doi.org/10.5066/P987S177.

Witter, R.C., Kelsey, H.M., Bender, A.M., Scharer, K.M., Lease, R.O., 2018. Repeated earthquake uplift at Icy Point, Glacier Bay National Park, Alaska: strain partitioning at a restraining bend in the Fairweather fault? Seismol. Res. Lett. 89, 836.

Witter, R.C., Bender, A.M., Scharer, K.M., DuRoss, C.B., Haeussler, P.J., Lease, R.O., 2021. Geomorphic expression and slip rate of the Fairweather fault, Southeast Alaska, and evidence for predecessors of the 1958 rupture. Geosphere 17 (3), 711–738.

Witter, R.C., Kelsey, H.M., Lease, R.O., Bender, A.M., Scharer, K.M., Haeussler, P.J., Brothers, D.S., 2023. Oblique Contraction along the Fastest Ocean-Continent Transform Plate Boundary Focuses Rock Uplift West of the Fairweather Fault, Southeast Alaska. AGU Monograph. In Press.

Wong, M.S., Gans, P.B., Roesler, D., 2023. Field calibration of 40Ar/39Ar K-feldspar multiple diffusion domain (MDD) thermal histories at the Grayback normal fault block, Arizona, USA. Geology 51 (9), 885–889.

Worthington, L.L., Van Avendonk, H.J., Gulick, S.P., Christeson, G.L., Pavlis, T.L., 2012. Crustal structure of the Yakutat terrane and the evolution of subduction and collision in southern Alaska. J. Geophys. Res. Solid Earth 117.

Wyld, S.J., Umhoefer, P.J., Wright, J.E., Haggart, J.W., Enkin, R.J., Monger, J.W.H., 2006. Reconstructing northern Cordilleran terranes along known cretaceous and Cenozoic strike-slip faults: implications for the Baja British Columbia hypothesis and other models. In: Paleogeography of the North American Cordillera: Evidence for and against Large-Scale Displacements: Geological Association of Canada Special Paper, 46, pp. 277–298.

Zhang, P., Jiang, S.Y., Donelick, R.A., Li, R., Soares, C.J., Mei, L., 2022. Frontal Expansion of an Accretionary Wedge under Highly Oblique Plate Convergence: Southern Indo-Burman Ranges. Geological Society of America Bulletin, Myanmar.